HHS Public Access

Author manuscript

NMR Biomed. Author manuscript; available in PMC 2017 January 19.

Published in final edited form as:

NMR Biomed. 2016 September ; 29(9): 1198–1221. doi:10.1002/nbm.3478.

Rapid brain MRI acquisition techniques at ultra-high fields

Kawin Setsompop[1,2], **David A. Feinberg**[3,4], and **Jonathan R. Polimeni**[1,2]

[1]Athinoula A. Martinos Center for Biomedical Imaging, Massachusetts General Hospital, Charlestown, MA, USA

[2]Department of Radiology, Harvard Medical School, Boston, MA, USA

[3]Helen Wills Institute for Neuroscience, University of California, Berkeley, CA, USA

[4]Advanced MRI Technologies, Sebastopol, CA, USA

Abstract

Ultra-high-field MRI provides large increases in signal-to-noise ratio as well as enhancement of several contrast mechanisms in both structural and functional imaging. Combined, these gains result in a substantial boost in contrast-to-noise ratio that can be exploited for higher spatial resolution imaging to extract finer-scale information about the brain. With increased spatial resolution, however, is a concurrent increased image encoding burden that can cause unacceptably long scan times for structural imaging and slow temporal sampling of the hemodynamic response in functional MRI—particularly when whole-brain imaging is desired. To address this issue, new directions of imaging technology development—such as the move from conventional 2D slice-by-slice imaging to more efficient Simultaneous MultiSlice (SMS) or MultiBand imaging (which can be viewed as “pseudo-3D” encoding) as well as full 3D imaging—have provided dramatic improvements in acquisition speed. Such imaging paradigms provide higher SNR efficiency as well as improved encoding efficiency. Moreover, SMS and 3D imaging can make better use of coil sensitivity information in multi-channel receiver arrays used for parallel imaging acquisitions through controlled aliasing in multiple spatial directions. This has enabled unprecedented acceleration factors of an order of magnitude or higher in these imaging acquisition schemes, with low image artifact levels and high SNR. Here we review the latest developments of SMS and 3D imaging methods and related technologies at ultra-high field for rapid high-resolution functional and structural imaging of the brain.

Keywords

CAIPIRINHA; *Simultaneous MultiSlice*; *MultiBand*; *blipped-CAIPI*; *3D imaging*; *3D-EPI*; *Wave-CAIPI*; *Simultaneous MultiSlice RF pulse design*

Corresponding Author Kawin Setsompop, Ph.D., Building 75, Room 2.102, 13th Street, Charlestown, MA, 02129, USA, kawin@nmr.mgh.harvard.edu.

1. INTRODUCTION

1.1. Benefits of high-resolution imaging

In recent years ultra-high field MRI has become widely adopted due to the substantial increases in image signal-to-noise ratio (SNR) and contrast-to-noise ratio (CNR) it affords, which can be exploited to reduce voxel sizes and increase resolution. In addition to the expected increased image SNR, several imaging modalities also enjoy a substantial boost in contrast with higher magnetic fields. For example, due to increased T_1 values in blood and tissue, there is an enhancement in the inflow effect that gives rise to time-of-flight angiography [1,2], and the longer blood T_1 values benefit perfusion measurements based on arterial spin labeling by prolonging the magnetization of the labeled blood enabling longer post-labeling delays [3–5]. Susceptibility-based contrasts such as T_2* are also enhanced at higher field strengths, providing improved depiction of iron-rich microanatomical features [6–8] and deoxyhemoglobin-rich small venules and veins [9,10]—as well as providing larger signal changes in blood-oxygen-level-dependent (BOLD) functional MRI (fMRI) [11].

While several early studies have already demonstrated the benefits of fMRI at ultra-high field strengths, there is an ongoing push to higher spatial and temporal resolutions to extract more information from fMRI measurements that is driving the expanded use of ultra-high field fMRI. Because BOLD CNR increases dramatically with field strength, fMRI studies at ultra-high field strengths typically take full advantage of this beneficial increased sensitivity by reducing the voxel size in order to measure finer structures of cortical and subcortical functional architecture. Not only do the smaller voxels allow for adequate spatial sampling of the cortical ribbon, but they also allow for sampling of even finer structures such as detailed topographic maps and the columnar architecture of the cerebral cortex [12–15]; these small voxels also create the ability to sample across various depths of the cortical gray matter to examine its laminar architecture [13,16–19], and to distinguish responses within small subcortical nuclei [20,21]. On the other hand, faster temporal sampling has also been demonstrated to increase the sensitivity in detecting brain networks in resting-state fMRI data [22] and provide the ability to achieve finer parcellations [23] as well as tracking of dynamic changes across these networks [24]. High spatial and high temporal resolution fMRI studies have been motivated in part by recent advances in optical imaging and microscopy that have provided new insights into neurovascular coupling, showing that hemodynamic responses to neural activity—which are the basis for fMRI—can be far more actively and precisely regulated in the brain than what was once believed (see [25] and references therein). There is now evidence for extremely fine-scale regulation within a capillary network [26] and mechanisms for rapid and precise blood flow regulation at the capillary level [27–30]. It is therefore expected that at microscopic spatial scales the hemodynamic response may in fact be extremely tightly coupled to the neuronal activity, implying that the specificity of the measured fMRI signals may be limited by the sensitivity with which we can detect changes and the spatiotemporal resolution used to measure these changes—both of which can be improved by moving to ultra-high field strengths. These new insights have opened the possibility to study the brain at the smallest levels of its functional architecture.

While there are clear advantages of ultra-high field MRI for several applications, there are some types of MR imaging that are hindered by contrast changes with magnetic field strength: short white matter T_2 values can cause signal reductions in diffusion MRI, short gray matter T_1 values can lower signal levels in rapid imaging, and low T_2* values can exacerbate blurring in many fMRI acquisitions with long echo train lengths. There are other challenges to moving to higher field strengths as well—such as the potential for greater imaging distortions and increased power deposition—that can place constraints on the imaging that can be performed. Each of these limitations can be alleviated with the development of faster image encoding techniques. Furthermore, because of the intensifying demand for both high spatial *and* high temporal resolution imaging, there has been a rapid emergence of new, fast image encoding paradigms to meet this mounting demand. New acquisition methods, including parallel imaging approaches and RF pulse design schemes, have been developed in order to meet these challenges. With these advanced imaging methods, one can begin to take full advantage of the sensitivity gains provided by ultra-high field strengths and allow high-quality, high-resolution imaging over the entire brain within a short time frame.

1.2. Rapid high-resolution imaging with Simultaneous MultiSlice and 3D imaging

Through the widespread availability of receive coil arrays, over the last decade parallel imaging (PI) technologies such as SENSE and GRAPPA [31–33] have enabled acceleration factors of 2–3× in routine clinical acquisitions. At ultra-high field strengths, coil sensitivity profiles exhibit increasing spatial variability, making the sensitivity profile of each element more distinct from the other elements in the array—which provides improved spatial encoding ability and allows for higher PI acceleration with low g-factor noise amplification [34–36]. With high-channel-count arrays, such as the 32-channel brain arrays that are now routinely used, acceleration factors of 4–5× are now readily achievable at ultra-high fields [37,38]. Nonetheless, high-quality imaging at extreme acceleration factors (>5×) in routine 2D slice-by-slice imaging has not been possible due to a combination of higher g-factor penalties and the intrinsic $\sqrt{R}$ SNR penalty, both of which increase with acceleration factor.

Volumetric 3D and SMS imaging, however, provide improved acceleration capability and improved SNR efficiency when compared to 2D slice-by-slice imaging. Both 3D and SMS acquisitions can be viewed as encoding data in 3D k-space rather than 2D k-space [39]. This enables improvements in PI reconstruction, since data under-sampling and hence image aliasing can be distributed into more spatial directions. Moreover, as an accelerated technique, SMS imaging has an important SNR advantage over 2D imaging. For SMS imaging, acceleration in the slice direction is performed by exciting proton spins of multiple slices simultaneously using MultiBand (MB) slice-selective pulses and recording their signals for the same duration as in an unaccelerated 2D scan [40]. This slice acceleration, unlike acceleration in 2D imaging, does not require omitting lines of k-space and thus does not incur the intrinsic $\sqrt{R}$ SNR penalty that occurs when the time window of signal accumulation for signal at each voxel of the imaging volume is shortened. The SNR advantage of eliminating the "√R penalty" can be particularly significant at high accelerations: for example, at R=9, the √R penalty alone leads to an SNR drop by a factor of 3 for 2D imaging. In the same manner as SMS imaging, 3D imaging is also more SNR

efficient than 2D imaging, since signal from an even larger portion of the imaging volume is being recorded at any given time to provide better noise averaging [41]. It was noted that the SNR benefit of 3D imaging sequences over their 2D counterparts can be diminished due to other sequence considerations (such as reduced signal recovery between acquisitions in tissues with long T_1 values), particularly in low spatial resolution acquisitions [42]. Considering the analysis presented in [42], this conclusion should also be true for SMS imaging sequences. However, for high-isotropic-resolution imaging, the SNR benefit from 3D and SMS imaging can be substantial [43].

The CAIPIRINHA "controlled aliasing" method, or CAIPI [44,45], has been proposed as technique to enable further improvement in PI performance for 3D and SMS imaging. This improvement is achieved by modifying the k-space under-sampling scheme to increase the spatial distance between aliased voxels in the reduced field-of-view (FOV) to allow for better use of coil sensitivity information. This class of techniques (which was proposed nearly a decade ago) has gained much interest in recent years due to a number of enabling developments, including the incorporation of CAIPI to rapid SMS-EPI (echo-planar imaging) acquisitions for fMRI and diffusion imaging, the development of low-Specific-Absorption-Rate (SAR) RF-pulses for SMS imaging, and new controlled aliasing acquisition and image reconstruction techniques which enable even higher accelerations.

In this review, we first focus on developments of rapid SMS and 3D imaging that have dramatically sped up acquisitions, particularly in fMRI and diffusion imaging. We then expand our scope into more recent extensions of rapid SMS and 3D acquisitions to structural imaging at ultra-high fields including T_2*, phase/QSM, magnetization-prepared rapid-acquisition gradient echo (MPRAGE), and rapid acquisition with relaxation enhancement (RARE) imaging. Additionally, a short discussion is devoted to low-SAR SMS RF pulse design that is critical for SMS imaging at ultra-high fields. Lastly, we provide an outlook on rapid imaging developments using SMS and 3D paradigms.

2. MAKING EPI FASTER

EPI is by far the most used pulse sequence for rapid imaging in functional, diffusion, and perfusion imaging. In this section, we will describe SMS and 3D extensions to EPI that have achieved acceleration factors of an order of magnitude or greater. We will also review technologies that have enabled these highly-accelerated imaging methods to be robustly applied and that have enabled rapid online image reconstruction, thereby allowing their widespread adoption. A survey of methods and results combining these techniques with other advanced acquisition strategies—to enable both rapid and high-quality high-resolution imaging at reduced levels of distortion and blurring—will also be provided.

2.1. Rapid Functional Imaging

2.1.1. SMS-EPI—PI was first incorporated into fMRI acquisitions as a way to reduce geometric distortions and T_2* blurring of 2D slice-by-slice EPI [46,47]. Because Blood-Oxygen-Level-Dependent (BOLD) fMRI acquisitions are constrained to use a TE value similar to the T_2* value of the brain region of interest (e.g., 20 ms for cortical gray matter at 7T [11]) to achieve optimal functional CNR, acceleration is not primarily used to increase

the sampling rate of the acquisition. Instead, acceleration benefits EPI quality by decreasing the effective echo-spacing to reduce geometric distortion (caused by susceptibility-gradient-induced B_0 inhomogeneity) and by shortening the echo-train length to reduce spatial blurring (caused by T_2* relaxation). Thus accelerating the EPI acquisition improves the spatial accuracy of the resulting images. With modern high-channel-count arrays, R_{inplane} acceleration factors of 3–5× are routinely used at ultra-high fields to provide high-quality, high-resolution imaging. Fig. 1 shows example data acquired with a 32-channel receive coil head array [48] and a head gradient coil, in this case single-shot BOLD-weighted gradient-echo EPI at 0.75 mm isotropic nominal resolution imaging acquired at R=3 acceleration. Head gradients allow for faster gradient switching and therefore more rapid image encoding due to the greatly reduced potential for peripheral nerve stimulation compared to body gradient coils that induce magnetic field gradients over the torso [49]. Nonetheless, to achieve a temporal sampling rate of at least 3–4 s with conventional single-slice imaging in order to adequately sample the hemodynamic response, only a small brain volume can be covered at such high resolution, limiting the use of small-voxel fMRI to partial-brain experiments. For example, at 1 mm isotropic resolution only a 4–5 cm section of the brain can be covered with a temporal sampling interval of 3–4 s.

Due in part to recent development efforts in support of the Human Connectome Project, SMS-EPI has become a key enabling technology for high-resolution fMRI acquisitions of the whole brain at rapid temporal sampling rates [50–52]. Over a decade ago, SMS acquisition using PI was first proposed by Larkman *et al*. [40] and demonstrated in leg imaging, and was later successfully adapted for EPI acquisitions of brain by Nunes *et al*. [53]. The SMS-EPI technique accelerates the EPI acquisition by acquiring multiple slices simultaneously, thereby covering the region of interest in fewer steps, and utilizing a receive coil array and PI reconstruction techniques to separate the multiple slices. Moeller *et al*. [54] first demonstrated the benefits of SMS-EPI (a.k.a. MultiBand EPI) for acquiring a larger number of thin slices for fMRI at 7T, while Feinberg *et al*. [22] achieved very fast temporal sampling for fMRI by imaging the whole brain in as little as 400 ms using the variant *Multiplexed* EPI that combines SMS-EPI with Simultaneous Image Refocusing (SIR) to provide increased slice acceleration factors. A major improvement was then achieved in reducing g-factor penalty in SMS-EPI to allow much higher slice accelerations (or MB factors) through the introduction of the blipped-CAIPI method [43], which enables Controlled Aliasing in SMS-EPI to increase the distance between the superimposed voxels. This is achieved by utilizing “blipped” gradient pulses on the G_s slice-select axis in addition to the phase encoding G_p blipped pulses during the EPI readout to create a phase modulation across the k-space data in order to impart a shift in the phase-encoding direction between simultaneously acquired slices, and to periodically refocus the accumulative effect of the blipped pulses to avoid the detrimental voxel “shearing” or blurring artifact seen in the previous effort [53]. The blipped-CAIPI method provides the ability to dramatically increase the number of simultaneous images read out in each single-shot EPI echo train; for example, with a 32-channel coil array at 3T, the achievable MB factor improves from 3× to 8× or higher when using the blipped-CAIPI scheme, enabling routine sub-second, whole-brain fMRI at 2 mm isotropic resolution [50].

One of the main applications of the rapid sampling offered by SMS-EPI is resting-state fMRI for functional connectivity studies, first demonstrated by Feinberg *et al.* [22], to increase the sensitivity of standard analysis methods to detect brain networks and later shown by Smith *et al.* [23] to enable the use of advanced analysis methods to provide finer parcellations. Fig. 2 shows recent functional connectivity results from a MB-12 fMRI acquisition using a custom-built 64-channel head-only helmet array coil [55] on the 3T Siemens "Connectom" system [52], where high-quality 2.5 mm isotropic whole-brain data were acquired with a TR of 350 ms. Fig. 2A shows results from standard seed-based functional connectivity analysis, which clearly identifies the Default Mode Network (DMN) from a MB-12 dataset of just 5-minute duration. Figs. 2B and 2C show an Independent Component Analysis (ICA) on the same dataset, where cardiac- and respiratory-driven fluctuations, as well as well-known whole-brain networks, are clearly and accurately identified as has been previously demonstrated [56].

To provide further accelerations, Multiplexed EPI, which combines multiband acceleration (MB) with SIR acceleration (S) to acquire a total of $N=S\times$MB images in each echo train, can be used [22]. The SIR method excites multiple image slices one at a time in sequential manner with gradient encoding in between each excitation to shift the k-space data from each slice along the frequency encoding direction thereby concatenating the multiple frames of k-space. To read out the k-space data from these frames SIR encodes across the expanded, concatenated k-space, which effectively interleaves the recording of the data from the multiple slices one line at a time. An important limitation of SIR is that it necessitates an elongation of the echo train by S times more echoes and an increase of the effective echo spacing for each image slice, which will increase distortions and potentially increase T_2* blurring. Higher spatial resolution imaging, which also necessitates increased encoding, is similar to SIR in its vulnerability to increased T_2* blurring due to the lower bandwidth (BW) of longer readout gradient pulses and the longer echo trains needed for the additional image encoding. Consequently it can become too demanding to achieve both high SIR accelerations and high spatial resolution as each acts to prolong echo train lengths, with compounding effects. The longer echo train length can be shortened by inplane acceleration to improve both distortions and blurring, as discussed below. Very recent comparisons of Multiplexed EPI at different acceleration factors were performed [57], where accelerations as high as $N=48$ was achieved to allow whole-brain imaging at $2.5\times2.5\times3$ mm^3 resolution in as fast as 100 ms at 3T with a 32-channel head coil (Fig. 3). Evaluation of time-series SNR (tSNR) as well as BOLD CNR and information content from visual cortical fMRI activation following stimulus presentation of a flashing checkerboard and movie clips showed that at low accelerations ($N \leq 6$), setting $S=1$ (i.e., no SIR encoding) and varying MB alone yielded the best results in all evaluation metrics. On the other hand, at higher accelerations ($N>8$), the use of $S=2$ yielded maximal BOLD CNR and information content as measured by classification of movie clip frames. Using SMS-EPI there is significantly greater BOLD information content at relatively fast TRs in the 300–600 ms range compared to a standard TR of 2 s, suggesting that such faster TRs provided with SMS-EPI captures more information per unit time in task-based fMRI.

As discussed above, for high-resolution imaging at ultra-high field conventional inplane PI acceleration is required to reduce image distortions and blurring. However the use of inplane

acceleration limits the slice acceleration capabilities because of the multiplicative interaction between undersampling in the inplane and slice directions. In our experience, high-quality acquisitions at a *total acceleration factor* ($R_{\text{inplane}} \times$ MB) of up to 14–16× are achievable with a 32-channel coil array at 7T for whole-brain protocols with blipped-CAIPI SMS-EPI. Fig. 4A shows the reconstruction of SMS-EPI at 1.5 mm isotropic resolution, acquired with 15× total acceleration (MB-5, R=3) using a custom 32-channel coil for 7T [48]. For this acquisition, the high inplane acceleration enables data acquisition at the optimal TE for BOLD contrast, and limits both T_2* blurring and B_0-inhomogeneity-induced image distortion, while the high MB acceleration allows fast temporal sampling of 1.2 s. At such high acceleration factors, the g-factor noise amplification penalty can be high, which reduces the achievable detection power in fMRI studies. This issue can be mitigated through the use of even larger channel-count receive arrays. Fig. 4B shows a simulation comparing 1/g-factor maps for MB-4 and MB-5 acquisitions, both with R=3 inplane, for an existing 32-channel array and for a hypothetical 128-channel coil array design for 7T. Significant reductions in noise amplification are seen with the 128-channel coil. For the MB-5 acquisition, the average and minimum 1/g-factors increase from 64% to 85% and 24% to 61% respectively.

2.1.2. SMS image reconstruction—A number of developments have been made to improve the quality and speed of SMS-EPI image reconstruction. The limitation of the original SENSE/GRAPPA approach for SMS reconstruction [58], which was initially not compatible with CAIPI shifting, has been overcome. SENSE/GRAPPA formulated the SMS reconstruction treating the simultaneously acquired slices as a concatenation along the phase encoding direction in image domain then Fourier transforms this composite image and separates the slices using GRAPPA, however when CAIPI shifting was employed image discontinuity artifacts could arise. The SENSE/GRAPPA method was later modified to provide artifact-free reconstructions when CAIPI shifting is applied through either (*i*) an extended FOV in the phase-encoded direction with additional zero-filled sections [59,60] or (*ii*) slice concatenation in the readout direction [61]. Slice-GRAPPA [43], which has been the most widely-used method for blipped-CAIPI SMS-EPI reconstruction, has also been refined to provide improved reconstruction with the “LeakBlock” technique [62]. This reconstruction reduces the leakage signal or cross-slice contamination between simultaneously acquired slices and has been shown to provide more temporally stable reconstructions at high accelerations, particularly in cases where both slice and inplane accelerations are employed. LeakBlock achieves this by formulating the slice-GRAPPA reconstruction of the separated slices from the collapsed slice group as a *filter* that explicitly minimizes leakage/residual aliasing across slices. For example, for MB=3 there will be three slice-GRAPPA kernel sets (one for each of the slices that are acquired simultaneously); the training forces the first kernel set, associated with the first slice, to act as a filter to pass-through the signal from the first slice and block out signals coming from the other two slices.

In examining signal leakage in SMS imaging, the L-factor as proposed by Xu *et al.* [63] is a useful summary metric for characterizing the signal leakage. The L-factor quantifies the residual artifacts present in separated slices; due to the linearity of the reconstruction

algorithms used for SMS imaging, this “leakage” is analogous to the residual aliasing artifact seen in inplane acceleration but now in the slice direction [62]. In this sense it is complementary to the g-factor in that it provides an error metric for the reconstruction. The L-factor quantifies this “slice aliasing” as the percentage of signal leakage from one of the simultaneously acquired slices into another slice. Based on this metric, Xu *et al.* [63] provide a useful empirical protocol design guideline based on their experiences with fMRI analysis of SMS-EPI data, and recommend limiting the mean L-factor to ≤ 0.05 and the maximum L-factor to ≤ 0.9. The L-factor can be reduced either by reducing the level of slice acceleration, by increasing the separation between collapsing slices, or by explicitly minimizing leakage through the use of advanced reconstruction algorithms—in particular we have found that both proposed modifications to the SENSE/GRAPPA technique (i.e., extended FOV in the phase encoding direction and slice concatenation in the readout direction) and the slice-GRAPPA with LeakBlock technique provide similarly good performance in terms of reducing L-factor caused by slice aliasing.

In another development, the SMS encoding process has also been presented as a 3D k-space encoding [39,64,65], which greatly simplifies the extension of SMS and CAIPI to non-Cartesian 3D sampling, and helps enable any of the established PI reconstruction methods to be applied to SMS data—opening new possibilities for SMS acquisition and image reconstruction development. Zahneisen *et al.* [66] showed that by appropriately adding `dummy slices' during the reconstruction, single-step SENSE can be used to perform reconstruction for SMS data with any combination of MB factor and CAIPIRINHA shift. Further, it was demonstrated that the exact same reconstruction could be applied to 3D CAIPI EPI data, which underscores the similarities between SMS and 3D acquisitions. The relationship between SMS and 3D encoding is considered further below in 3D-EPI with CAIPI sampling and its relation to SMS-EPI with blipped-CAIPI.

The amount of data acquired with SMS and 3D EPI acquisitions can be large. Approaches for near/real time-reconstruction of highly-accelerated SMS-EPI acquisition have been developed to aid in monitoring patient compliance and quality control. The use of GPU cards and remote reconstruction computation with specialized computer and networking hardware developed by the University of Minnesota group have allowed for rapid reconstruction [51]. Fast image reconstruction computations based on an efficient coil compression method proposed by Zhang *et al.* [67] have also recently been developed to provide near/real time reconstruction using standard CPU hardware on commercial scanners, with no noticeable degradation in image quality or SNR [68].

Although many recent advances in SMS reconstruction were motivated by EPI-based acquisitions, these strategies (such as slice-GRAPPA with LeakBlock) can be applied to SMS acquisitions integrated into other pulse sequences for structural imaging—these structural applications of SMS acquisitions are considered in ***SMS for structural imaging***.

2.1.3. PI calibration data acquisition for SMS-EPI—To enable widespread and routine usage of SMS-EPI, it is crucial to achieve high acceleration factors robustly. The acquisition of high-quality PI reference (a.k.a. Auto-Calibration Signal or ACS) data plays an important role in producing high-quality reconstructions, particularly in the presence of

motion. For high-resolution whole-brain SMS imaging, reference data scans can be lengthy (on the order of 30 s or longer), which enhances the vulnerability to motion and/or dynamic B_0 changes (due to e.g. subject respiration) already inherent in standard inplane segmented multi-shot EPI ACS acquisitions [69]. For EPI with inplane accelerations FLASH-based ACS [70,71] has been shown to yield improved SNR in the EPI time-series [72] and provide a far more robust reconstruction in the presence of small changes during the reference data acquisition, such as those driven by respiration or eye movements [69,73] when compared to standard multi-shot EPI ACS. This FLASH-ACS acquisition has been extended to SMS-EPI with both slice and inplane acceleration [73]. However, the robustness and high SNR of a FLASH-ACS does come at a cost of image geometry mismatch to the distorted EPI time-series data, which could result in suboptimal unaliasing performance and thus increased ghosting artifacts. An alternative reference scan approach based on the Fast Low-angle Excitation Echo-planar Technique (FLEET) method [74] has been proposed, which overcomes this issue. The FLEET approach is a reordered version of multi-shot EPI with drastically reduced motion vulnerability achieved by acquiring all EPI segments of a given slice in a rapid, sequential manner [69]. Because each segment is typically acquired in less than 50 ms, there is very little time for longitudinal magnetization recovery between the acquisition of each segment, therefore the FLEET method evenly distributes the available magnetization across segments by utilizing low-angle excitations, similar to the FLASH method—in this sense, FLEET can be viewed as a “turbo” FLASH sequence in which all lines within a slice are acquired before moving on to the next slice. Variable flip-angle versions of this acquisition are also possible in which the flip angle is slowly increased across segments as a function of the recovery time and the expected T_1 value of the tissue [75–77], however the success of this approach hinges upon accurate flip angles over the object and similar slice profiles for each flip angle to ensure that the segments are compatible with one another [69]. A potential limitation of the FLEET method is that the reduced flip angles result in lower signal levels, which may impact PI calibration for high-resolution ACS acquisitions where SNR is already scarce.

FLEET-ACS data is distortion-matched to the EPI time-series data, and has been shown to provides improved unaliasing performance in the presence of strong B_0 inhomogeneity [69]. This method has also been extended to SMS-EPI calibration for slice and inplane acceleration via “SMS-FLEET”, which reorders the acquisition of the uncollapsed set of training images such that all slices corresponding to a collapsed slice group in the SMS-EPI data are acquired sequentially before moving to the next slice group [78]. Such EPI-based reference scans have been shown to provide robust, high-quality reconstruction even when the subject is instructed to deliberately move during the reference scans [78], as demonstrated in Fig. 5.

The majority of research into generating robust reference data for SMS-EPI has been focused on trying to achieve the best autocalibration data for k-space based reconstruction such as GRAPPA and slice-GRAPPA. This path of development has been shaped as a result of GRAPPA-based reconstructions being the main reconstruction approach used thus far for these acquisitions. It is possible that the effects of motion sensitivity and geometric distortion in reference data might manifest themselves somewhat differently in image-domain reconstruction approaches such as SENSE—where the reference data are used to

explicitly estimate coil sensitivities in the image domain rather than to fit convolution kernels in k-space—and this remains to be explored. However, we note that, as with k-space based reconstruction methods, in SENSE it is desirable to have reference scan data that have matching geometric distortion to the accelerated image data, and also at ultra-high fields the reference data should be acquired at relatively high spatial resolution to capture more rapid coil sensitivity variation over space [79], particularly with high-channel-count arrays utilizing small detectors. Therefore, it is likely that multi-shot EPI data would be a suitable reference data acquisition method for SENSE-based reconstructions of SMS-EPI as well. Thus the use of methods such as FLEET to circumvent motion sensitivity of multi-shot EPI acquisition should also be helpful for sensitivity profile information in SENSE-based reconstructions.

2.1.4. SMS and CAIPI extensions: spiral and segmented-EPI—Recently SMS acquisition has been extended to multiple-slice spiral imaging [65,80,81], where efforts have been made to adopt Controlled Aliasing through the use of a sinusoidal G_z waveform [80] and a blipped G_z waveform (termed blipped-Spiral) [81,82], both of which act to smear out the aliasing between the SMS slices, with the later showing good-quality reconstructions of MB-8 data at 3T.

Multi-shot segmented EPI for 2D imaging is an alternate strategy to inplane parallel imaging for decreasing the geometric distortion and T_2* blurring in EPI time-series data by dividing each image into multiple short readouts [83]. However, due to the dynamic phase changes over the brain and cerebrospinal fluid spaces driven by motion or subject respiration, phase errors are often seen between interleaves, causing temporally unstable ghosting in the reconstructed image series. The FLEET approach, mentioned above in the context of PI calibration data, overcomes these phase misalignments by minimizing the time interval between segments. Another approach to reducing the time interval between segments is to employ SMS techniques to speed up the time required to encode the stack of images, thereby reducing the TR. This Multi-Shot SMS-EPI has been demonstrated to improve image quality and time-series SNR over conventional Multi-Shot EPI [84]. This example demonstrates how the faster acquisition by SMS-EPI can be exploited to improve image quality or to make time to acquire complementary images. This principle has also been applied to cluster-volume acquisitions [85,86] as well as multiple-echo acquisitions [87,88], each of which require additional encoding time. In both cases, the SMS-EPI acquisition can reduce the imaging time per volume to enable these techniques to acquire whole-brain data quickly.

2.1.5. 3D-EPI with CAIPI sampling and its relation to SMS-EPI with blipped-CAIPI—Segmented 3D-EPI has been applied successfully at ultra-high field to provide high-quality, high-resolution fMRI with lower SAR penalty and with reduced spin-history artifact in the presence of subject motion when compared to conventional 2D-EPI acquisitions [89,90] since with each shot a full 3D volume is excited. Similar to SMS-EPI, for 3D-EPI the acceleration in the k_z partition encoding direction leads to a reduction in the minimum TR by $1/R$, thus acceleration applied in this encoding scheme can similarly be used to increase temporal resolution. Recent incorporation of CAIPI into 3D-EPI has

enabled far higher accelerations of up to 16× at 7T [91,92], similar to what is achieved with blipped-CAIPI SMS-EPI. Fig. 6 shows imaging results from two different k-space under-sampling schemes of 16× accelerated 3D-EPI with CAIPI at 7T: $R_y \times R_z = 4\times4$ (top row) and 16×1 (bottom row). The 0.8 mm isotropic data exhibited low levels of distortion with a short TR of only 1.99 s using a 4×4 acceleration scheme. With the 16×1 scheme, the short TR (and reduced segmentation) was traded off for a much shorter echo-train length of 12 ms, which is highly favorable for multi-echo imaging and provides further reductions in image distortion. This example highlights the ability of 3D-EPI with CAIPI in using coil sensitivity variations in both y and z directions to accelerate the acquisition in a flexible manner.

Both SMS-EPI and 3D-EPI benefit from CAIPI encoding strategies to increase acceleration capabilities. As mentioned above, a close link exists between the CAIPI approaches applied to “pseudo-3D” SMS and full 3D acquisitions [39,64,65]. In SMS-EPI with blipped-CAIPI, the G_s blips impose a phase variation along the slice direction akin to phase encoding along the k_z direction of 3D-EPI. Fig. 7 shows the 3D k-space sampling of SMS-EPI with blipped-CAIPI at $R_{inplane}$×MB = 2×8 and an inter-slice image shift of FOV/4 (corresponding to FOV/2 in the reduced inplane FOV) in the center blue highlighted region of k-space. This k-space sampling pattern is identical to the k-space sampling pattern of the 3D-EPI with CAIPI at $R_y \times R_z = 4\times4$ in Fig. 6, where the CAIPI shift causes the aliasing voxels to originate from 8 different z positions rather than 4. With the same k-space sampling pattern, both the 3D-EPI and the SMS-EPI acquisitions exhibit identical aliasing patterns. In the SMS-EPI case, it is sufficient to encode only the center portion of k-space since the MultiBand pulse excites a subset of the 3D imaging volume and causes the effective spatial resolution along z (i.e., $k_{z,\max\ SMS}$) to decrease to match the distance between simultaneously excited slices. Here, the sampling of standard 2D-EPI, which samples only along k_z=0, is modified by blipped-CAIPI to create a more uniform sampling density along k_z within the blue highlighted region. This creates an inter-slice image shift of FOV/2 (with respect to the reduced FOV caused by $R_{inplane}$=2) to provide a more favorable distribution of the image aliasing. From this viewpoint, the “pseudo-3D” encoding used by SMS-EPI can be considered as a single-shot acquisition that is intermediate between standard 2D EPI and multi-shot 3D EPI—in 2D-EPI only a single k_z line is sampled, and in 3D-EPI k-space is sampled out to $k_{z,\max\ 3D}$, whereas in SMS-EPI sampling along k_z is only extended to $k_{z,\max\ SMS}$. The MultiBand pulses in SMS-EPI therefore allow a smaller region of k-space along k_z to be sampled compared to 3D-EPI.

For the 3D-EPI with $R_y \times R_z = 4\times4$, the B_0 inhomogeneity related image distortion will be halved that of the SMS-EPI with $R_{inplane}$×MB = 2×8 due to its 2× higher inplane undersampling. On the other hand, a 3D-EPI with $R_y \times R_z = 2\times8$ that acquires two k_z partitions per EPI shot using same blipped trajectory as the SMS-EPI acquisition (with an additional initial k_z partition encoding) will have both the same image distortion and the same aliasing pattern as the aforementioned $R_{inplane}$×MB = 2×8 SMS-EPI, while providing 2× faster acquisition relative to 3D-EPI at $R_y \times R_z = 4\times4$. For the same FOV_z coverage, this 3D-EPI acquisition also consists of the same number of EPI readout trains as the aforementioned SMS-EPI acquisition, and therefore these 3D-EPI and SMS-EPI acquisitions should have the same TR.

Given the similarity of the image encoding and controlled aliasing in blipped-CAIPI SMS-EPI and accelerated 3D-EPI with CAIPI, the main difference between the two acquisitions is that SMS-EPI acquires each slice group in a single shot (i.e., it encodes all of the excited spins after each shot), whereas 3D-EPI requires multiple shots to encode the entire volume. The choice between using 3D-EPI versus SMS-EPI is mainly in the trade-off between improved signal averaging in 3D-EPI at a cost of increased physiological noise from such multi-shot acquisitions, which will be application dependent. While 3D acquisitions can provide increased image SNR, it has been shown that the maximum available temporal SNR in 3D-EPI is reduced compared to single-shot acquisitions, and this reduction increases with increased segmentation, thus is likely due to physiological noise processes [90]. Image-based physiological noise correction though recording of pulse and respiration has been proposed to allow increase in tSNR of 3D-EPI [93]. Moreover, a number of recent methods have been developed that can be used to enable large reductions in segmentation and hence acquisition time and physiological noise contamination of 3D-EPI. In addition to the use of CAIPI sampling, the use of UNFOLD in 3D-EPI [94] has also been proposed for reducing segmentation. 3D reduced-excitation (RE)-EPI [95], which encodes two k_z planes per segment, could also provide further reduction—albeit at a cost of increased image distortion. Synergistic combination of these accelerated techniques for 3D-EPI will be an interesting avenue of future research. Lastly, we note that CAIPI has also been extended to multi-shot stack-of-spiral acquisition for fMRI [96] to reduce the number of segments analogously to its use in 3D-EPI [97].

2.1.6. Selective excitation in Zoomed EPI—Similar to segmented imaging, Zoomed Imaging is an important strategy for reducing the image encoding burden and thereby achieving very-high resolution functional or diffusion imaging of the brain with sub-millimeter voxel sizes. This is achieved by overcoming the limitation that the image FOV normally must cover an entire brain cross-section to prevent aliasing wraparound artifacts. Zoomed imaging encodes a smaller sub-region of the brain without reducing the image matrix to more finely sample the brain region for higher spatial resolution (i.e., by using a bigger Δk to cover a larger k-space extent)—and, similar to a zoom lens on a camera, the FOV is proportionally reduced with zooming. In MRI acquisitions, the signal-producing region generated by the RF transmission must be limited to match the smaller FOV of the encoded image otherwise unwanted signal outside of the FOV will alias or overlap onto the primary image.

The earliest approach to zoomed MRI, Inner Volume Imaging (IVI) [98]—as the name implies—utilizes orthogonal, directed excitation and refocusing slabs to generate spin-echo signal only within the intersecting region—i.e., the slice lying at the intersection between orthogonal excitation slab and refocusing slab—where zoomed imaging is performed with 2D or 3D spin-echo EPI; in this approach, however, multiple-slice or multiple-slab acquisitions are not possible. For example, if the excitation slab were positioned axially and the refocusing slab were positioned coronally, after the intersection region is encoded it is not straightforward to immediately excite a second axial slab directly above or below the encoded intersection region because all spins within the coronal slab have experienced the refocusing pulse and therefore have reduced magnetization. Inner-volume EPI [99], later

referred to as “Zonal-EPI” or “Zoomed-EPI” by Mansfield and colleagues [100], is similarly limited because intrinsically it can only generate a single slice within each TR. To overcome this limitation, 3D volume-zoomed sequences excite a larger volume that can be encoded using two phase-encoding axes.

A commonly used approach to zoomed imaging operates by restricting the volume of signal via suppressing signals outside of the image FOV, and therefore goes by the name “outer volume suppression” (OVS) but is now also often referred to as Zoomed-EPI. The suppression pulse designs currently in use were originally formulated by Luo *et al.* [101] and were demonstrated by Pfeuffer *et al.* for zoomed 7T imaging [102]. Ultra-high spatial resolution of human brain at 7T using IVI for zoomed 3D spin-echo EPI has been combined with OVS pulses at the slab edge to sharpen the slab boundary and reduce the need for oversampling to achieve 300 μm inplane resolution and 2 mm thick slices for exquisite, detailed images of the basal nuclei and brainstem [103]. This zoomed-EPI approach is hindered at ultra-high fields by the resulting higher levels of SAR stemming from the repeated application of a suppression pulse needed for each imaging slice (in addition to any excitation or refocusing pulses) to maximize the suppression effect and to prevent T_1 signal recovery. Zoomed parallel imaging (ZOOPPA) EPI [104] combines OVS with GRAPPA to achieve 0.65 mm isotropic resolution fMRI at low distortion. Recently OVS-zoomed SMS-EPI or Zoomed MB Imaging (ZOMBI) up to an acceleration of 6 (R=2, MB-3) has also been used for high-resolution fMRI [105]. The utility of SMS is that it enables SAR reduction in OVS-zoomed imaging, because the SAR reduction achieved from requiring fewer OVS pulses (by a factor equal to the MB factor) outweighs the SAR increase from the use of MB excitation pulses.

A useful differentiation can be made between the application of inner volume excitation to SE-based sequences and outer volume suppression to GE sequences. The IVI approach can only be used in SE sequences because it uses an orthogonal orientation the excitation or refocusing slabs, and since these slabs will excite/refocus regions outside of the intersection region all tissue within these slabs must undergo full longitudinal magnetization recovery, which in effect prevents multiple-slice or multiple-slab imaging. Although OVS also uses a suppression pulse this is typically applied within the excited slab, but not above or below, hence it allows for multiple-slice or multiple-slab imaging. Therefore zoomed imaging with SE-EPI and 3D GRASE encoding using IVI is limited to a single slice or single volume, whereas the zoomed GE-EPI with OVS and can be performed with multiple-slice imaging.

All zoomed methods restrict the imaging to a specific brain region of interest in order to reduce encoding or acquisition time. Recently Finsterbusch [106] has generalized this notion by using 2D spatially-selective RF pulses to encode multiple zoomed regions spatially separated from each other, allowing for zooming in more complex fMRI experiments studying multiple brain regions simultaneously while providing very rapid sampling rates. This can be a great advantage in experiments in which the locations of the activated brain areas are known *a priori*. Nonetheless, as with many zoomed techniques, it also requires somewhat long RF pulse durations to achieve the custom 2D spatial patterns of selection, which places constraints on the minimal TE that can be achieved.

2.1.7. Selective excitation and selective refocusing in 3D GRASE imaging—At ultra-high field strengths spin-echo contrast has been proposed as a method to increase the specificity of the BOLD signal by reducing extravascular effects [107–109]. The gradient-and-spin-echo (GRASE) pulse sequences [110] provide T_2 weighting and the desired spin-echo BOLD contrast through a 3D EPI readout that incorporates 180° refocusing pulses between EPI segments. Because multiple gradient echo lines comprising an EPI segment are read out with each refocusing, this approach requires fewer refocusing pulses than traditional spin-echo-based echo-train methods such as RARE, and therefore deposits less energy and results in reduced SAR. A key advantage of the 3D GRASE technique is its ability utilize IVI, as described above, to effectively zoom the acquisition in two directions in order to limit the amount of image encoding required. To further decrease image encoding time, conventional PI acceleration can also be incorporated. One potential drawback of the 3D GRASE technique applied at ultra-high field strengths is that the many refocusing pulses can lead to SAR limitations, even with the small number of refocusings between the EPI readouts. However the application of single-shot 3D-GRASE for sub-millimeter zoomed fMRI has been largely unhampered by SAR limits because these high-resolution acquisitions typically target small brain regions amenable to zooming and, therefore, a small amount of image encoding resulting in extremely fast 3D acquisitions. Thus in practice a time series of 3D-GRASE pulse sequence measurements includes a relatively long period when no RF pulses are applied, which reduces SAR at the expense of lower time efficiency and/or reduced temporal sampling rates. However, for SE-based imaging, the lengthened TR allows for T_1 recovery to enable good SNR efficiency when TR is in the range of 1.5–2.5 s for these zoomed acquisitions. Therefore, zoomed single-shot 3D-GRASE, which employs orthogonal oriented excitation and refocusing slabs with intervening EPI-like encoding has become very useful for fMRI at ultra-high field [111] where the spin-echo contrast provided by 3D GRASE appears favorable for increasing the spatial specificity of the BOLD responses. Zoomed 3D-GRASE has produced highly-sensitive spin-echo based BOLD contrast to depict the functional organization of the middle temporal visual cortical area (area MT) [112] (Fig. 8), the tonotopic arrangement in primary auditory cortex within cortical layers [113], and layer-specific computational modeling in the neocortex [16]—all at 7T ultra-high field.

Recently, the use of multiple intersecting RF slabs created by orthogonal MB slab-selective excitation pulses and orthogonal single-band refocusing pulses in zoomed 3D-GRASE has enabled *Simultaneous Multi-Volume* imaging [114,115]. Furthermore, a promising extension to IVI 3D-GRASE—which incorporates a variable refocusing flip angle scheme to help prolong the signal during readout and counterbalance T_2 decay and consequent blurring effects in GRASE by promoting stimulated echo contributions to the signal—has been proposed that allows for encoding of additional slice partitions and results in a narrower PSF along the secondary phase encoding direction [116]. Another promising 3D variant is *Simultaneous Multi-Slab* EVI [117] which was shown to increase volume coverage up to 3× with MB-3 pulses.

2.2. Rapid Perfusion Imaging

Ultra-high fields also provide a contrast boost for perfusion imaging due to greatly increased blood T_1, tissue T_1, and the reduced T_2* of injected contrast agents along with the increased SNR, all of which can be exploited for increases in sensitivity or spatial resolution. However, challenges in B_1^+ and B_0 inhomogeneity, short tissue T_2* values, and high SAR has presented a challenge to Arterial Spin Labeling (ASL) at 7T, nevertheless there is a growing number of studies developing and utilizing ASL at ultra-high field strengths [4,118–122].

Recently Blipped-CAIPI SMS-EPI has been shown to benefit ASL-based perfusion measurements at high fields [123,124]. Because after labeling the blood longitudinal magnetization (and therefore the perfusion signal) decays with time constant T_1, the imaging slices must be acquired as quickly as possible following the tag, and the time taken for the labeled blood in the neck to travel to the brain is controlled solely by the vascular system. Therefore many ASL studies are restricted to adopt a small number of slices in order to both capture the labeled blood before the longitudinal magnetization returns to equilibrium and to minimize the difference in post-labeling delays experienced by each acquired slice. SMS-EPI methods help to reduce both of these problems. Although accelerated PI methods are often not advocated for ASL due to the inherently low SNR in the resulting cerebral blood flow (CBF) maps, an advantage of SMS PI methods is the lack of the $\sqrt{R}$ penalty, and therefore the SNR losses in SMS image reconstructions are minor. One drawback to SMS-EPI applied to ASL is that labeled blood traveling up from the neck to the brain will experience the MultiBand excitation pulses before the magnetization reaches the final imaging slices, which for quantitative CBF maps will have to be taken in account.

With SMS techniques, promising high-resolution whole-brain pseudo-continuous ASL (pCASL) data have been acquired at 7T including pCASL FLASH with MB-5 [125] and whole-brain SMS-EPI with MB-6 [126], where SMS acquisitions significantly reduce inversion time variability and reduce SNR losses along the slice direction due to T_1 decay in the labeled blood. Additionally, ASL with multi-echo SMS-EPI has also been achieved at 7T [127], where in addition to MB-3, inplane acceleration of 2 was used to achieve short echo train to enable the acquisition of multiple echoes. Such sequence improvements should enable concurrent whole-brain CBF and BOLD measurements.

Blipped-CAIPI SMS-EPI has also been incorporated into Dynamic Susceptibility Contrast imaging (DSC) [128,129] to allow for increased brain coverage and/or increased slice resolution while retaining the needed high temporal sampling rate. Here, adequate temporal sampling rate is necessary for accurate estimation of perfusion measures from the temporal profile of the contrast bolus [130], which can be difficult to achieve with whole-brain coverage using conventional single-band acquisitions.

2.3. Rapid Diffusion Imaging at Ultra-High Fields

Like functional and perfusion imaging, diffusion imaging at ultra-high field enjoys the benefit of higher intrinsic SNR, which ideally would provide the extra sensitivity needed for higher-resolution imaging. However, this benefit comes with a number of significant

challenges including: shorter T_2 values in brain tissue which dramatically reduce signal levels; increased B_0 spatial inhomogeneity which increases EPI geometric distortion; B_1^+ spatial inhomogeneity which can cause large spatially varying flip angle, particularly problematic in spin-echo acquisitions; and lastly high SAR penalties at ultra-high field. Due partly to these reasons, recent diffusion acquisition development efforts (e.g. those from the NIH Human Connectome projects) have been mainly focused at 3T using powerful gradient systems and acquiring data at very high b-values [52,131], with recent effort now being extended to high-resolution diffusion 7T [132]. Nevertheless, a number of high-quality, high-resolution diffusion imaging studies have been performed at 7T, with early initial efforts from Mukherjee *et al.* and Poupon *et al.* [133,134]. The main developments over the last few years at 7T have been to further reduce echo spacing and echo-train length of EPI by augmenting inplane PI [135–137] and partial Fourier approaches with zoomed imaging and multi-shot segmented methods. By shortening the TE of the diffusion-weighted acquisition, these techniques mitigate the effect of shorter T_2 values, and in some accelerated PI cases [136] the gain in signal level from the short TE overcomes the $\sqrt{R}$ SNR loss, PI can result in a net SNR gain. Partial Fourier, however, is more conventionally used to reduce TE —at the expense of lost image spatial resolution, particularly when zero-filled reconstruction is used. Accelerated PI, zoomed imaging, and segmented methods also act to reduce geometric distortion—caused by both eddy current effects and B_0 inhomogeneity—and chemical shift artifacts through decreasing the effective echo spacing. Use of powerful gradient hardware has also provides further benefits such as shorter achievable diffusion encoding times as well as reduced echo-spacing for high-resolution imaging. Reduced-FOV and segmented EPI have been utilized successfully to provide high-resolution diffusion imaging at 7T, albeit at long scan times which in some cases last up to an hour or longer. Blipped-CAIPI SMS-EPI has been shown to speed up diffusion imaging by a factors of 3–4 with minor noise amplification penalty [138], while higher accelerations, as with fMRI, are not feasible due to the associated noise amplification penalty that is detrimental to the SNR-starved diffusion imaging. Recently, Blipped-CAIPI SMS-EPI has been successfully incorporated into both reduced-FOV and segmented EPI with initial demonstrations provided at 7T. A detailed review of these developments at ultra-high fields is provided below.

A large number of zoomed imaging methods have been proposed for diffusion imaging, with a recent study providing a thorough comparison of eight of these methods applied at 7T [139]. A number of studies have demonstrated zoomed imaging for diffusion imaging at 7T, all of which rely on OVS combined with partial Fourier acquisition and accelerated PI. The first of these studies applied this technique to diffusion weighted imaging (DWI) to reduce distortion artifacts and improve imaging of the temporal and frontal lobes regions that are in close proximity to large air-tissue interfaces [140]. A similar strategy, which has been termed ZOOPPA, was developed and applied to acquire partial-brain coverage of ultra-high spatial and angular resolution diffusion imaging at 7T, achieving an impressive 800 μm isotropic resolution at b=1000 s/mm^2 with an effective acceleration factor of 4.6× ($R_{\text{inplane}} \times R_{\text{zoom}} = 3 \times 1.53$) to provide low-distortion data [141] (see Fig. 9). The resulting high-quality data highlight the benefits of ultra-high-field diffusion imaging, and was successfully used to resolve complex and subtle fiber architectures including fiber crossings in the white

matter, anisotropy in the cortex, and fibers entering into the cortex. Similar techniques have also recently been applied to highly-localized high-resolution DTI of the midbrain and brainstem, achieving high-quality low-distortion data in this difficult to image region [142,143].

The time efficiency of zoomed diffusion imaging has recently been increased through the simultaneous acquisition of multiple imaging slices. Saritas *et al.* utilized a 2D spatially-selective RF pulse to limit the imaging field-of-view while also simultaneously exciting multiple imaging slices of the spinal cord at 1.5T, which were then unaliased using classic Hadamard encoding and related reconstruction techniques [144]. Such methods provide an improvement in SNR efficiency and a reduction in acquisition time. However, the scan time reduction benefit of such methods is limited to acquisitions that utilize multiple averages per diffusion direction. Moreover, Eichner *et al.* combined ZOOPPA with blipped-CAIPI SMS-EPI to provide large reduction in scan time and improve SNR efficiency of high-resolution, low-distortion diffusion data at 7T [145]. This acquisition was made possible through the use of PINS refocusing pulses [146], which significantly reduce the high SAR of MB refocusing pulses (and are discussed further below in RF PULSE DESIGN FOR SMS: issues of SAR, peak power and B_1^+ inhomogeneity). We note that such acquisitions can be further optimized for rapid *whole-brain* diffusion by using outer-volume suppression in ZOOPPA to suppress signal from the neck and mouth region and changing the phase encoding direction to oblique head-foot direction, as depicted in Fig. 10.

Similar to zoomed EPI, multi-shot EPI sequences provide the ability to achieve high-resolution diffusion imaging, but they come at a significant cost of increased scan time. Readout segmented EPI (rs-EPI) with PI [147–149], which segments the EPI acquisition in the frequency-encoding direction rather than in the conventional phase-encoding dimension, has been successfully applied at 7T for high-resolution diffusion imaging [150]. To reduced scan time rs-EPI has also been combined with partial Fourier [151] and blipped-CAIPI SMS to provide more rapid diffusion imaging acquisition at both 3T and 7T [152]; in this same theme, Peterson *et al.* [153] also demonstrated SMS with rs-EPI at 3T. Additionally, conventional multi-shot EPI has been successfully employed at 7T for high-resolution diffusion imaging by relying on 2D phase-correction navigators (needed to correct spatially-varying phase errors across the image in diffusion imaging) and an image-space sampling function (IRIS) reconstruction method—a modified SENSE reconstruction technique that accounts for shot-to-shot 2D phase errors [154]. Moreover, the multiplexed sensitivity encoding (MUSE) method has been proposed to correct shot-to-shot 2D phase variations in conventional multi-shot EPI without the use of navigators and demonstrated for high inplane resolution diffusion imaging at 3T [155]. MUSE modifies the SENSE reconstruction to allow joint reconstruction of multiple EPI segments using an assumption that the shot-to-shot phase variations are spatially smooth. Removing the need for navigators is important, since navigators reduce the time efficiency of multi-shot diffusion imaging and typically require a second 180° pulse which can increase SAR penalty significantly at ultra-high field. The multi-shot MUSE method has been extended to be compatible with SMS and partial Fourier techniques, with fast high inplane resolution diffusion imaging demonstrated at 3T [156]. In this method, the CAIPI FOV-shift in the SMS acquisition was achieved using RF

phase cycling between EPI segments, analogous to the scheme used in the original CAIPIRINHA proposal for SMS-GRE (gradient-recalled echo) acquisitions [44].

Other recent developments in fast diffusion imaging have exploited q-space Compressed Sensing (CS) acquisition and reconstruction [157–162] present another interesting avenue of research, which enables acceleration along an axis orthogonal to k-space for further accelerating diffusion imaging with SMS-EPI. Q-space CS and k-space SMS-EPI have been shown to synergistically combine to provide more than an order of magnitude acceleration in diffusion imaging [52,163], which should prove to be highly beneficial to lengthy, high-resolution diffusion imaging at ultra-high fields.

3. STRUCTURAL IMAGING

In functional, diffusion, and perfusion imaging one of the main goals of rapid acquisition techniques is to increase temporal resolution, brain coverage, and time efficiency. In structural imaging, faster acquisitions can also increase time efficiency, enabling more contrasts to be acquired at higher spatial resolution for richer anatomical information in a time-frame suitable for *in vivo* imaging. In this realm of anatomical imaging, the most common use of ultra-high-field MRI has been to produce high-resolution imaging, taking advantage of both the intrinsic boost in image SNR as well as the boost in contrast seen in, e.g., T_2* and time-of-flight contrast. Higher resolution allows for detecting small intracranial blood vessels [1,2,164], finer sampling of the cortical ribbon required for cortical thickness measurements [165], for identifying brain areas on the basis of their microanatomy [166–168], for delineating subcortical nuclei [169], and for building accurate brain atlases [170]. These high-resolution acquisitions are required for accurate delineation of the brain tissues needed for many functional and anatomical studies. However, to successfully achieve high-resolution imaging requires long encoding and acquisition times, which potentially lead to vulnerability to subject motion, dynamic physiological changes, and to sources of image blurring and other artifacts that corrupt the accuracy and reduce the resolution of the final images. Here we review rapid acquisition techniques that not only shorten scan times to increase scanning efficiency but that also enable concurrent imaging of multiple image contrasts and provide higher quality data through reducing vulnerability to motion, artifacts arising from dynamic physiological changes, and blurring that accumulates with time during the image encoding.

3.1. SMS for structural imaging

One domain in which faster 2D acquisitions can improve image quality is in cardiac-gated imaging. Cardiac pulsation artifacts are somewhat more challenging to remove in anatomical imaging. Synchronizing the acquisition to the cardiac signal (measured through, e.g., pulse oximetry) can remove these artifacts, however this strategy can be prohibitively time-consuming for 3D structural imaging since it forces the timing of the acquisition to match that of the cardiac cycle, which in humans has a period of about 0.8 s. One typical approach to incorporate cardiac gating into high-resolution imaging is through slice-interleaved 2D multi-slice acquisitions, in which case the TR is constrained by the period of the cardiac cycle—which limits the number of slices that can be acquired, restricting brain coverage.

The SMS technique with CAIPI FOV shifting can be used to extend this high-quality 2D imaging to a larger imaging volume. An example of an ultra-high resolution cardiac-gated 2D GRE acquisition at 7T, using slice-GRAPPA reconstruction, is shown in Fig. 11.

Bulk head motion can also be the source of image artifacts, and longer encoding times prolong the period of a scan session that is vulnerable to inevitable patient motion; although at higher field strengths sufficient SNR may be available for small-voxel acquisitions motion vulnerability during long encoding times can be a limiting factor. SMS acquisitions can also be applied to accelerate 2D anatomical imaging in order to provide high spatial resolutions over the entire brain in clinically-acceptable scan times. An application of blipped-CAIPI to SMS-RARE imaging has been demonstrated for T_2-weighted imaging at 7T with MB-8 acceleration achieved at acceptable SAR level through the use of PINS pulses [146,171], which are described in greater detail in Sec. 4. In RARE imaging the phase of the refocusing pulses must be cycled during the echo train to satisfy the Carr-Purcell-Meiboom-Gill (CPMG) condition, and it is possible to simultaneously impose the necessary slice-specific phase modulation across k-space to achieve CAIPI FOV shifting when using conventional MultiBand pulses since each band can be assigned a fixed phase offset for each echo train. On the other hand, the simultaneous phase cycling and FOV shifting via RF phase modulation is less straightforward to achieve when using PINS pulses. Here, however, the blipped-CAIPI technique can be adopted to provide a straightforward way to create FOV shifting [171].

3.2. Accelerating during inversion recovery: CAIPI-MPRAGE and MEMPxRAGE for quantitative T_1 3D imaging

Acceleration can also be employed in some cases to reduce image blurring artifacts in 3D imaging. To enhance image contrast, many 3D structural imaging techniques, such as MPRAGE, utilize magnetization preparation pulses and typically many k-space partitions are encoded after each pulse [172]. Relaxation and recovery effects cause a modulation of the k-space data, resulting in a loss of spatial resolution. While strategies exist to tailor the RF excitation pulse train to mitigate these smoothing effects [173,174], the success of the flip angle schedules is largely determined by the accuracy of the assumed relaxation parameters (e.g., T_1, and T_2) and by how closely the desired flip angle can be achieved throughout the brain. An alternate strategy to reduce blurring during these long readout trains is to accelerate the image encoding immediately following each magnetization preparation pulse. This is in distinction to the conventional way in which acceleration is used in MPRAGE—typically the outer loop of the image encoding is accelerated by undersampling in the phase-encoding direction (thus playing fewer magnetization preparation pulses) to reduce scan time. Similar to inplane-accelerated EPI, this new “inner-loop” acceleration strategy is primarily employed to reduce blurring, and not to reduce scan time. Inner-loop acceleration has been used in combination with the GRAPPA PI method to achieve 350 μm isotropic T_1-weighted MPRAGE at 3T [175]. With reduced readout durations, multiple readouts can be included after each magnetization preparation, each with a different inversion time and therefore different image contrast weighting. This strategy was demonstrated recently in a novel “MEMPxRAGE” acquisition [176], which extends both multi-echo MPRAGE (or MEMPRAGE [177]) and double-inversion-time MPRAGE

(MP2RAGE [178]), but allows for an arbitrary number of effective inversion times. This provides a more time-efficient encoding scheme in which data is acquired throughout more of the inversion recovery period. These multiple images can also be used to compute quantitative T_1 maps by fitting a signal model based on the Bloch equations to the multiple TI data [176]. High quality MPRAGE with accelerations in both the inner and the outer loop can be achieved via 2D-CAIPIRINHA, which aids in reducing g-factor noise amplification. An example of a CAIPI-MEMPRAGE image—using R_{pe}=3 for outer-loop acceleration and R_{par}=2 for inner-loop acceleration—acquired at 3T with a 32-channel coil is presented in Fig. 12, demonstrating the feasibility of such an approach to reduce both image blurring artifacts (by 2×) and scan time (by 3×) through PI. Such rapid acquisition technique is expected to be very beneficial to high-spatial-resolution imaging favored at ultra-high fields.

3.3. 3D gradient echo imaging: phase imaging and QSM

Many forms of tissue contrast are accentuated at ultra-high fields, providing increased image CNR which can enable smaller voxels and a more accurate depiction of the fine-scale anatomy, however, high-resolution acquisitions can be extremely encoding intensive and lengthy—particularly when multiple contrasts are required for the more advanced quantitative methods that provide improved image quality and/or additional useful information. Phase imaging, Susceptibility-Weighted Imaging (SWI) and Quantitative Susceptibility Mapping (QSM) have been shown to provide dramatic improvement in CNR [179–182] at ultra-high fields, yielding exquisite intracortical and subcortical contrast [6,7]. The desire for sub-millimeter resolution and requirement of long TE to build up phase contrast between tissues for improved CNR both contribute to long imaging time. For QSM, which has the benefit of mitigating the misleading orientation bias of phase imaging and SWI, whole-brain coverage is required to enable the deconvolution step in the reconstruction needed to calculate the underlying tissue magnetic susceptibility from the observed tissue phase, which further adds to the image encoding burden. For QSM, the susceptibility is calculated by taking into account the “dipole” magnetic field pattern emanating from oriented structures, but this calculation is inherently ill-posed due to singularities in the Fourier transform of the dipole field [183] leading to streaking artifacts which can be mitigated through regularization [181,184,185], at a cost of some spatial blurring. A more thorough approach to overcome the ill-posed reconstruction of the susceptibility map is to acquire the image data when the subject repositions their head in multiple orientations relative to the main magnetic field [186]. Multi-orientation QSM can be extremely time consuming, but has yielded enhanced tissue contrast and detailed depiction of deep gray matter structures at 7T [187,188]. Moreover, it has been shown that tissue magnetic susceptibility can be orientation dependent and anisotropic [189–192], leading to the development of Susceptibility Tensor Imaging (STI) [190]. STI requires sampling at even more head orientations (e.g. N>10), lengthening the scan time which makes it impractical for *in vivo* human imaging. Recent proposals constrain the reconstruction using prior information derived from diffusion tensor imaging (DTI) [191], and thus reduce the sampling requirement to N=3–4 orientations. Such prior information proved especially useful at 7T *in vivo* [192], where the tight-fitting modern 32-channel head array coils constrain the attainable angle relative to the main field to remain relatively low.

At sub-millimeter resolution, the encoding-intensive requirements for phase and QSM imaging (as well as for T_2* weighted imaging) can lead to extremely lengthy acquisitions if the standard GRE-based acquisition approach is used. This has led several groups to investigate the use of EPI-based acquisition approaches. EPI can be used to speed up the acquisition but comes at the cost of artifacts compared to conventional GRE acquisitions. A modified interleaved-segmented-EPI sequence has been proposed for SWI that uses a reconstruction method to correct for phase variation in presence of moderate field inhomogeneities [193]. Moreover, multi-shot stack-of-spiral has also been used to accelerate T_2*/phase imaging to achieve 1 mm isotropic multi-echo data within 2.5 min at 3T [194]. Recently, short-axis propeller (SAP)-EPI [195] has been extended to 3D and used for SWI acquisitions [196], achieving whole-brain 0.94×0.94×2 mm resolution in less than 2 minutes at 3T, with motion-correction capability. At ultra-high fields, highly-segmented 3D-EPI [197] was successfully employed to provide rapid 0.5 mm isotropic whole brain acquisition in 6 min at 7T with relatively low distortion (BW in the phase-encoding direction of 41 Hz/pixel). Moreover, with 3D whole-brain imaging, acceleration in two directions using PI to substantially reduce acquisition time is possible. This has been exploited in standard GRE acquisitions [198] as well as in 3D-EPI [199,200] for SWI. The use of 2D-CAIPIRINHA in 3D-EPI, recently demonstrated for fMRI [91,92], will be a promising direction to explore in providing higher accelerations for effective susceptibility imaging.

3.4. Wave-CAIPI for rapid SMS and 3D structural imaging

With the success of CAIPI sampling for SMS and 3D imaging, new efforts have been made to extend the CAIPI principle to all three spatial encoding dimensions. The “Wave-CAIPI” method, named for its sinusoidally-varying G_y and G_z gradients played during frequency encoding, has recently been proposed as a way to allow even greater PI acceleration through controlled aliasing [201]. The Wave-CAIPI technique synergistically combines k-space under-sampling of 2D-CAIPIRINHA [45] and a modified version of Bunched Phase Encoding/Zig-Zag sampling [202,203] to create a staggered corkscrew trajectory (Fig. 13A), which maximizes the distance between aliased voxels in all three spatial dimensions (*x*-*y*-*z*) and can be adapted for 3D as well as SMS accelerated acquisitions, where for the SMS acquisition the recent 3D k-space encoding view can be employed [39,64,65]. Fig. 13B shows the inter-slice shift along *y* between aliased slices in *z* caused by staggered k_y-k_z sampling of 2D-CAIPIRINHA and the position-dependent voxel spreading along *x* resulting from G_y and G_z gradients of the corkscrew trajectory. These effects combine to create a complex aliasing pattern in an accelerated acquisition (Fig. 13B, center), which can be resolved using an efficient SENSE-based reconstruction that incorporates information about the modified k-space sampling and trajectory [201] (Fig. 13B, right). We note that a precursor to Wave-CAIPI was proposed by Breuer [204] through a simulation demonstrating that a 2D CAIPIRINHA acquisition with an alternating, zig-zag shift by Δk_y and Δk_z during the readout can provide markedly improved parallel imaging performance when compared to standard 2D CAIPIRINHA. The controlled aliasing in all three spatial dimensions of Wave-CAIPI has been shown to enable an order-of-magnitude increase in acquisition speed with minimal noise amplification and artifact penalty [201]. Wave-CAIPI should therefore enable rapid and highly-accelerated acquisitions of structural imaging in both SMS and 3D encoding paradigms. In particular, Wave-CAIPI is well suited for the relatively low

bandwidth readout of structural imaging at e.g. 100–400 Hz/pixel, enabling large corkscrew trajectories to be used to effectively spread out the voxel aliasing.

The dramatic acceleration achieved by Wave-CAIPI is possible by taking advantage of the relatively low bandwidth acquisition in many structural imaging sequences, which allows more k-space encoding to be performed. The corkscrew-like constant-rate trajectory was chosen to enable simple SENSE-based reconstruction without the need for gridding. Importantly, with this trajectory, unlike other rapid acquisitions (such as EPI, spiral, or their multi-shot variants), Wave-CAIPI provides a rapid acquisition without undesirable image distortion/blurring from B_0 inhomogeneity. This is because Wave-CAIPI traverses k-space in the readout direction with the same constant rate as conventional acquisitions, with B_0 inhomogeneity-related phase evolving solely as a function of k_x. Note that these desirable properties of requiring a simple reconstruction while not introducing image blurring would also be achieved with other "Wave" trajectories along k_y-k_z that are periodic with constant rate of k_x traversal, and provides room for further optimization and investigation.

For 3D-GRE based acquisitions, the Wave-CAIPI controlled aliasing method has recently been used to provide high acceleration factors with negligible noise amplification at 7T [201]. This enables high-quality acquisitions of 0.5 mm isotropic whole-brain 3D-GRE for QSM in just 5 minutes. Fig. 13C shows results from this acquisition, where high-quality tissue phase, QSM and SWI can be obtained from these data. Additionally, Wave-CAIPI has also recently been applied to accelerate multi-head orientation QSM acquisition at 3T [205].

3.5. New directions in rapid multi-modal and Quantitative MRI

It has long been recognized that quantitative MRI techniques can provide more detailed information about the underlying tissue properties, and the higher SNR available at ultra-high fields has helped push renewed efforts into developing quantitative techniques, however quantitative imaging and parameter mapping often require multiple measurements with varying image contrasts, prolonging scan times. The EPI-based technological developments outlined in previous sections have made dramatic improvements in EPI resolution and data quality. While these developments were driven by functional, diffusion, and perfusion imaging applications, the resolution of the EPI data is now higher than many standard anatomical scans, and many groups are moving towards using EPI-based imaging for anatomical imaging as well. The benefit of this approach is that the functional data and the structural data (as well as perfusion and diffusion data) can have identical image encoding and therefore will be perfectly geometrically matched. This concept has been recently applied for matching functional data with anatomical data used for automatic tissue segmentation and cortical surface reconstruction [206] as well as for a multi-modal EPI examination consisting of anatomical, functional, diffusion, and phase imaging of the human brainstem [207]. The fast readouts and high temporal efficiency of SMS-EPI also allow for efficient acquisition of multiple image contrasts that can be used for quantitative measurements of tissue relaxation parameters, such as the multi-echo SMS-EPI discussed above [208,209] used to separate neuronal effects from physiological noise in BOLD imaging as well as for rapid quantitative T_1 mapping *in vivo* [210,211].

The new, innovative concept of MR fingerprinting [212] is another promising approach to rapid quantitative MRI. MR fingerprinting involves generation of temporally and spatially incoherent signal evolutions, or fingerprints, for different tissue types through continuous variation of the acquisition parameters, such as the flip angle (FA), RF phase, TR and k-space sampling pattern. A template-matching algorithm is then used to match the fingerprints to a predefined dictionary of predicted signal evolution. The MR parameter maps, such as T_1, T_2, off-resonance and proton density (M_0), are estimated as values providing the best signal template match. One key advantage of MR fingerprinting at ultra-high fields is its ability to model sources of image artifacts such as B_0 and B_1^+ inhomogeneity and thereby remove these confounds from the final parameter maps. An innovative modification of MR fingerprinting method has also recently been developed and applied at 7T and 9.4T in the presence of B_1^+ field inhomogeneity for rapid simultaneous T_1 mapping and B_1^+ mapping of multiple transmit coils in a parallel transmission system [213].

4. RF PULSE DESIGN FOR SMS: issues of SAR, peak power and B_1^+ inhomogeneity

The success of all of the SMS techniques reviewed here hinges upon careful design and implementation of RF pulses. SMS imaging is typically performed using MB excitation pulses, which can have high peak power and high SAR levels—particularly for high MB factors. This can act as a roadblock in performing high-MB SMS imaging at ultra-high fields. Peak power of MB pulses can be reduced by a phase optimization scheme [214] and/or a pulse time-shift method [215] to allow the high-power peaks of the MB sub-pulses to not add constructively. We note that these methods were originally proposed more than two decades ago: for application of chemical shift imaging in the case of phase optimized scheme [216], and for Hadamard imaging and spectroscopy in the case of pulse time-shift method [217,218]. Additionally, we note that the small delays added between the multiple bands in the time-shift method can result in differences in the time-to-echo between the MB slices. However, in the context of diffusion imaging using bipolar diffusion-encoding gradients and spin-echo acquisitions [219,220] this can be overcome by modifying the relative time shift applied to the 90° and the 180° pulses [215]. A similar strategy can also be applied to acquisitions utilizing monopolar diffusion-encoding gradients [221], but comes at a cost of differences in effective TE between the MB slices.

Further reductions of peak power have also recently been reported for the case of spin-echo acquisitions through combining the phase optimization scheme of Wong *et al.* with the use of 90° excitation and 180° refocusing slice-selective pulses with spatially-varying excitation phases (through-slice) that combine to provide a flat spin-echo excitation phase [222,223]. Although these methods successfully reduce peak power, they do not reduce SAR. The VERSE algorithm, which slows the traversal through excitation k-space at high-peak-power locations by modifying the gradient waveform played during the RF pulse, can be used to reduce both peak power and SAR of MB pulses [138,224], but comes at the cost of slice-profile distortion in the presence of off-resonance as well as increased pulse duration. The Power Independent of Number of Slices (PINS) RF pulse design [146] has been proposed as a strategy to excite/refocus a large number of imaging slices simultaneously without

increasing peak power or SAR. The PINS pulse creates a periodic slice excitation pattern suitable for SMS imaging through performing a constant under-sampling of a single-slice RF pulse and depositing the corresponding RF energy at discrete, equally-spaced locations in the excitation k-space. PINS has been successfully employed in diffusion [145] and RARE imaging [171] at high MB factors at 7T. However, PINS pulses have the disadvantage of limited time-bandwidth product. Furthermore, these pulses can be particularly lengthy for thin-slice imaging, and reducing their duration increases SAR and peak power, diminishing the benefit of these pulses. MultiPINS pulses [225] combine PINS and MB pulse designs to further reduce peak power and SAR by up to 40–50%, which can be traded off for shorter pulse duration as demonstrated in SMS diffusion imaging at 7T. In MultiPINS design, the MB RF-pulse is reshaped using the VERSE algorithm to allow its segments across excitation k-space to be played out during the RF dead-times of the PINS pulse while a G_s gradient blip is applied to traverse between equally spaced locations in excitation k-space. This strategy eliminates the RF dead-times of the PINS pulse and enables PINS and MB pulses to be played out in an interleaved fashion to synergistically share the load in performing the excitation. k_T-PINS [226], a hybrid of PINS and the k_T-point [227] method, has also been proposed as a way to achieve low SAR SMS excitations with B_1^+ inhomogeneity correction, which can be important at ultra-high field, albeit at a cost of increasing PINS pulse duration even further.

Parallel Transmission (pTx) techniques [228–230] have recently been employed to improve SMS imaging. RF shimming of MB RF pulses with slice-specific shim weights in a full parallel transmission mode (pTx-MB) has been used to provide reduced RF power and improve excitation homogeneity at 7T [231]. RF power reduction of MB pulses has also been achieved at 3T by exploiting the spatially localized transmission profiles of dual-ring transmit coil arrays [232]. Subsequent work via electromagnetic field simulations also show large benefit of such dual-ring transmit coil designs for pTx-MB pulses at 7T [233].

MB RF pulse design for SMS applications is a rapidly growing research topic with new contributions from many groups; we summarize some notable examples here. MB RF pulses incorporating “fast-k_z” or “spoke” designs [234,235] have been proposed and demonstrated for brain imaging at 3T [236] and 7T [237] to allow SMS imaging with B_1^+ inhomogeneity mitigation. To further reduce SAR and improve excitation homogeneity, these methods have also been combined with parallel transmission design (pTx-Spoke-MB), along with peak power constraints in the RF pulse design [238,239] as well as a full, explicit peak power and local SAR constraints design [240]. In the work by Guérin *et al.* and Sharma *et al.* [239,240], the magnitude-least-squares design [241] was also incorporated to provide further power and local SAR reduction. Lastly, Spectral-Spatial designs [242] have also been incorporated into SMS excitation in both MB and PINS pulse designs to reduce susceptibility-induced signal loss artifacts in gradient-echo EPI near regions of severe B_0 inhomogeneity [243], and have been combined with efficient selective-excitation z-shimming technique [244]. Some of these new pTx-based SMS pulse designs have recently been employed for rapid imaging at ultra-high field, including pTx-MB employed for MB-4 diffusion imaging at 7T [245] and pTx-Spoke-MB employed for MB-2 cardiac CINE imaging at 7T [246].

5. CONCLUSIONS AND OUTLOOK

Ultra-high-field MRI provides dramatic gains in CNR for many forms of functional and structural imaging that can be exploited for high-resolution brain imaging, however small-voxel, whole-brain acquisitions place a heavy burden on the image encoding that can be met in part by increasing acquisition speed. New, promising directions of pulse sequence and image reconstruction design to provide rapid acquisitions include the move from conventional 2D slice-by-slice imaging to both SMS and highly-accelerated 3D imaging that are capable of more fully utilizing the spatial encoding power of the receive coil array through controlled aliasing in multiple spatial dimensions. These developments combined with new methodologies to reduce image artifacts in rapid acquisitions for e.g. EPI and Spiral has allowed high quality, high resolution imaging at a much faster timeframe. A summary of rapid brain acquisition sequence developments and their benefits are provided in Table 1. Further, advances in MRI hardware technology that are now on the horizon—including not only massively parallel, dense receive coil arrays but also new fast, strong gradient coil designs for faster image encoding, novel B_0 shim array designs [247–249] and magnetic field probes to adaptively mitigate B_0 inhomogeneity in real time [250–252], and novel pTx coil design approaches and increased pTx channel count—are all able to relieve some of the encoding burden from the accelerated parallel imaging and will enable even further acquisition accelerations in the near future. The pace of RF pulse design for SMS acquisitions, often utilizing pTx technology, has also quickened recently, and new strategies for using these pulses not only for B_1^+ nonuniformity mitigation but also potentially for image encoding can also contribute to pushing the limits of rapid acquisition especially at ultra-high field. These new technologies can be combined synergistically to offer exciting possibilities for robust, rapid image acquisitions with high spatiotemporal sampling to explore the fine-scale organization and function of the brain.

ACKNOWLEDGEMENTS

We would like to thank Dr. André van der Kouwe for providing the CAIPI-MEMPRAGE pulse sequence and Dr. Himanshu Bhat for providing the SMS-FLEET ACS pulse sequence. We would also like to thank Drs. Boris Keil and Thomas Witzel for 7T scanning assistance and support, and Dr. Larry Wald for helpful comments. We also thank the anonymous reviewers for their helpful suggestions. This research was provided in part by the NIH National Institute for Biomedical Imaging and Bioengineering (P41-EB015896, R00-EB012107, K01-EB011498, and R01-EB019437) and National Institute of Neurological Disease and Stroke (NIH R44 NS073417). Additional support was provided by the NIH Blueprint for Neuroscience Research (U01-MH093765), part of the multi-institutional Human Connectome Project.

REFERENCES

1. Zwanenburg JJM, Hendrikse J, Takahara T, Visser F, Luijten PR. MR angiography of the cerebral perforating arteries with magnetization prepared anatomical reference at 7 T: comparison with time-of-flight. Journal of Magnetic Resonance Imaging. 2008; 28(6):1519–26. PMID: **19025959**. [PubMed: 19025959]
2. von Morze C, Xu D, Purcell DD, Hess CP, Mukherjee P, Saloner D, Kelley DAC, Vigneron DB. Intracranial time-of-flight MR angiography at 7T with comparison to 3T. Journal of Magnetic Resonance Imaging. 2007; 26(4):900–4. PMID: **17896360**. [PubMed: 17896360]
3. Pfeuffer J, Adriany G, Shmuel A, Yacoub E, Van de Moortele P-F, Hu X, Uğurbil K. Perfusion-based high-resolution functional imaging in the human brain at 7 Tesla. Magnetic Resonance in Medicine. 2002; 47(5):903–11. PMID: **11979569**. [PubMed: 11979569]

4. Gardener AG, Gowland PA, Francis ST. Implementation of quantitative perfusion imaging using pulsed arterial spin labeling at ultra-high field. Magnetic Resonance in Medicine. 2009; 61(4):874–82. PMID: **19189295**. [PubMed: 19189295]
5. Golay X, Petersen ET. Arterial spin labeling: benefits and pitfalls of high magnetic field. Neuroimaging Clinics of North America. 2006; 16(2):259–68. PMID: **16731365**. [PubMed: 16731365]
6. Duyn JH, van Gelderen P, Li T-Q, de Zwart JA, Koretsky AP, Fukunaga M. High-field MRI of brain cortical substructure based on signal phase. Proceedings of the National Academy of Sciences of the United States of America. 2007; 104(28):11796–801. PMID: **17586684**. [PubMed: 17586684]
7. Fukunaga M, Li T-Q, van Gelderen P, de Zwart JA, Shmueli K, Yao B, Lee J, Maric D, Aronova MA, Zhang G, Leapman RD, Schenck JF, Merkle H, Duyn JH. Layer-specific variation of iron content in cerebral cortex as a source of MRI contrast. Proceedings of the National Academy of Sciences of the United States of America. 2010; 107(8):3834–9. PMID: **20133720**. [PubMed: 20133720]
8. Langkammer C, Krebs N, Goessler W, Scheurer E, Yen K, Fazekas F, Ropele S. Susceptibility induced gray-white matter MRI contrast in the human brain. NeuroImage. 2012; 59(2):1413–9. PMID: **21893208**. [PubMed: 21893208]
9. Haacke EM, Mittal S, Wu Z, Neelavalli J, Cheng Y-CN. Susceptibility-weighted imaging: technical aspects and clinical applications, part 1. AJNR. American Journal of Neuroradiology. 2009; 30(1): 19–30. PMID: **19039041**. [PubMed: 19039041]
10. Koopmans PJ, Manniesing R, Niessen WJ, Viergever MA, Barth M. MR venography of the human brain using susceptibility weighted imaging at very high field strength. Magnetic Resonance Materials in Physics, Biology and Medicine (MAGMA). 2008; 21(1–2):149–58. PMID: **18188626**.
11. Yacoub E, Shmuel A, Pfeuffer J, Van de Moortele P-F, Adriany G, Andersen P, Vaughan JT, Merkle H, Uğurbil K, Hu X. Imaging brain function in humans at 7 Tesla. Magnetic Resonance in Medicine. 2001; 45(4):588–94. PMID: **11283986**. [PubMed: 11283986]
12. Yacoub E, Harel N, Uğurbil K. High-field fMRI unveils orientation columns in humans. Proceedings of the National Academy of Sciences of the United States of America. 2008; 105(30): 10607–12. PMID: **18641121**. [PubMed: 18641121]
13. Polimeni JR, Fischl B, Greve DN, Wald LL. Laminar analysis of 7T BOLD using an imposed spatial activation pattern in human V1. NeuroImage. 2010; 52(4):1334–46. [PubMed: 20460157]
14. Sanchez-Panchuelo RM, Besle J, Beckett A, Bowtell R, Schluppeck D, Francis S. Within-digit functional parcellation of Brodmann areas of the human primary somatosensory cortex using functional magnetic resonance imaging at 7 tesla. Journal of Neuroscience. 2012; 32(45):15815–22. PMID: **23136420**. [PubMed: 23136420]
15. Hoffmann MB, Stadler J, Kanowski M, Speck O. Retinotopic mapping of the human visual cortex at a magnetic field strength of 7T. Clinical Neurophysiology. 2009; 120(1):108–16. PMID: **19071059**. [PubMed: 19071059]
16. Olman CA, Harel N, Feinberg DA, He S, Zhang P, Uğurbil K, Yacoub E. Layer-specific fMRI reflects different neuronal computations at different depths in human V1. PloS one. 2012; 7(3):e32536. PMID: **22448223**. [PubMed: 22448223]
17. Koopmans PJ, Barth M, Norris DG. Layer-specific BOLD activation in human V1. Human Brain Mapping. 2010; 31(9):1297–304. PMID: **20082333**. [PubMed: 20082333]
18. Trampel R, Bazin P-L, Schäfer A, Heidemann RM, Ivanov D, Lohmann G, Geyer S, Turner R. Laminar-specific fingerprints of different sensorimotor areas obtained during imagined and actual finger tapping. Proc Intl Soc Mag Reson Med. 2012; 20:663.
19. Siero JCW, Petridou N, Hoogduin H, Luijten PR, Ramsey NF. Cortical depth-dependent temporal dynamics of the BOLD response in the human brain. Journal of Cerebral Blood Flow and Metabolism. 2011; 31(10):1999–2008. PMID: **21505479**. [PubMed: 21505479]
20. Satpute AB, Wager TD, Cohen-Adad J, Bianciardi M, Choi J-K, Buhle JT, Wald LL, Barrett LF. Identification of discrete functional subregions of the human periaqueductal gray. Proceedings of the National Academy of Sciences of the United States of America. 2013; 110(42):17101–6. PMID: **24082116**. [PubMed: 24082116]

21. De Martino F, Moerel M, Van de Moortele P-F, Uğurbil K, Goebel R, Yacoub E, Formisano E. Spatial organization of frequency preference and selectivity in the human inferior colliculus. Nature Communications. 2013; 4:1386. PMID: **23340426**.
22. Feinberg DA, Moeller S, Smith SM, Auerbach EJ, Ramanna S, Gunther M, Glasser MF, Miller KL, Uğurbil K, Yacoub E. Multiplexed echo planar imaging for sub-second whole brain FMRI and fast diffusion imaging. PloS one. 2010; 5(12):e15710. PMID: **21187930**. [PubMed: 21187930]
23. Smith SM, Miller KL, Moeller S, Xu J, Auerbach EJ, Woolrich MW, Beckmann CF, Jenkinson M, Andersson J, Glasser MF, Van Essen DC, Feinberg DA, Yacoub ES, Ugurbil K. Temporally-independent functional modes of spontaneous brain activity. Proceedings of the National Academy of Sciences of the United States of America. 2012; 109(8):3131–6. PMID: **22323591**. [PubMed: 22323591]
24. Lee H-L, Zahneisen B, Hugger T, LeVan P, Hennig J. Tracking dynamic resting-state networks at higher frequencies using MR-encephalography. NeuroImage. 2013; 65:216–22. PMID: **23069810**. [PubMed: 23069810]
25. Devor A, Sakadžić S, Srinivasan VJ, Yaseen MA, Nizar K, Saisan PA, Tian P, Dale AM, Vinogradov SA, Franceschini MA, Boas DA. Frontiers in optical imaging of cerebral blood flow and metabolism. Journal of Cerebral Blood Flow and Metabolism. 2012; 32(7):1259–1276. PMID: **22252238**. [PubMed: 22252238]
26. Chaigneau E, Oheim M, Audinat E, Charpak S. Two-photon imaging of capillary blood flow in olfactory bulb glomeruli. Proceedings of the National Academy of Sciences of the United States of America. 2003; 100(22):13081–6. PMID: **14569029**. [PubMed: 14569029]
27. Murphy DD, Wagner RC. Differential contractile response of cultured microvascular pericytes to vasoactive agents. Microcirculation. 1994; 1(2):121–128. PMID: **8790583**. [PubMed: 8790583]
28. Peppiatt CM, Howarth C, Mobbs P, Attwell D. Bidirectional control of CNS capillary diameter by pericytes. Nature. 2006; 443(7112):700–4. PMID: **17036005**. [PubMed: 17036005]
29. Hamilton NB, Attwell D, Hall CN. Pericyte-mediated regulation of capillary diameter: a component of neurovascular coupling in health and disease. Frontiers in Neuroenergetics. 2010; 2:1–14. PMID: **20725515**. [PubMed: 20162100]
30. Hall CN, Reynell C, Gesslein B, Hamilton NB, Mishra A, Sutherland BA, O'Farrell FM, Buchan AM, Lauritzen M, Attwell D. Capillary pericytes regulate cerebral blood flow in health and disease. Nature. 2014; 508(7494):55–60. PMID: **24670647**. [PubMed: 24670647]
31. Pruessmann KP, Weiger M, Scheidegger MB, Boesiger P. SENSE: sensitivity encoding for fast MRI. Magnetic Resonance in Medicine. 1999; 42(5):952–62. PMID: **10542355**. [PubMed: 10542355]
32. Sodickson DK, Manning WJ. Simultaneous acquisition of spatial harmonics (SMASH): fast imaging with radiofrequency coil arrays. Magnetic Resonance in Medicine. 1997; 38(4):591–603. PMID: **9324327**. [PubMed: 9324327]
33. Griswold MA, Jakob PM, Heidemann RM, Nittka M, Jellus V, Wang J, Kiefer B, Haase A. Generalized autocalibrating partially parallel acquisitions (GRAPPA). Magnetic Resonance in Medicine. 2002; 47(6):1202–10. PMID: **12111967**. [PubMed: 12111967]
34. Wiesinger F, Van de Moortele P-F, Adriany G, De Zanche N, Uğurbil K, Pruessmann KP. Parallel imaging performance as a function of field strength--an experimental investigation using electrodynamic scaling. Magnetic Resonance in Medicine. 2004; 52(5):953–64. PMID: **15508167**. [PubMed: 15508167]
35. Pruessmann KP. Parallel imaging at high field strength: synergies and joint potential. Topics in Magnetic Resonance Imaging. 2004; 15(4):237–244. [PubMed: 15548954]
36. Ohliger MA, Grant AK, Sodickson DK. Ultimate intrinsic signal-to-noise ratio for parallel MRI: electromagnetic field considerations. Magnetic Resonance in Medicine. 2003; 50(5):1018–30. PMID: **14587013**. [PubMed: 14587013]
37. Wiesinger F, Zanche N. De, Pruessmann KP. Approaching Ultimate SNR with Finite Coil Arrays. Proc Intl Soc Mag Reson Med. 2005; 13:672.
38. Keil B, Wald LL. Massively parallel MRI detector arrays. Magnetic Resonance in Medicine. 2013; 229:75–89. PMID: **23453758**.

39. Zahneisen B, Poser BA, Ernst T, Stenger VA. Three-dimensional Fourier encoding of simultaneously excited slices: generalized acquisition and reconstruction framework. Magnetic Resonance in Medicine. 2014; 71(6):2071–81. PMID: **23878075**. [PubMed: 23878075]
40. Larkman DJ, Hajnal JV, Herlihy AH, Coutts GA, Young IR, Ehnholm G. Use of multicoil arrays for separation of signal from multiple slices simultaneously excited. Journal of Magnetic Resonance Imaging. 2001; 13:313–317. PMID: **11169840**. [PubMed: 11169840]
41. Brunner P, Ernst RR. Sensitivity and performance time in NMR imaging. Journal of Magnetic Resonance. 1979; 33:83–106.
42. Johnson G, Wadghiri YZ, Turnbull DH. 2D multislice and 3D MRI sequences are often equally sensitive. Magnetic Resonance in Medicine. 1999; 41(4):824–8. PMID: **10332860**. [PubMed: 10332860]
43. Setsompop K, Gagoski BA, Polimeni JR, Witzel T, Wedeen VJ, Wald LL. Blipped-controlled aliasing in parallel imaging for simultaneous multislice echo planar imaging with reduced g-factor penalty. Magnetic Resonance in Medicine. 2012; 67(5):1210–24. PMID: **21858868**. [PubMed: 21858868]
44. Breuer FA, Blaimer M, Heidemann RM, Mueller MF, Griswold MA, Jakob PM. Controlled aliasing in parallel imaging results in higher acceleration (CAIPIRINHA) for multi-slice imaging. Magnetic Resonance in Medicine. 2005; 53:684–691. PMID: **15723404**. [PubMed: 15723404]
45. Breuer FA, Blaimer M, Mueller MF, Seiberlich N, Heidemann RM, Griswold MA, Jakob PM. Controlled aliasing in volumetric parallel imaging (2D CAIPIRINHA). Magnetic Resonance in Medicine. 2006; 55(3):549–56. PMID: **16408271**. [PubMed: 16408271]
46. de Zwart JA, van Gelderen P, Kellman P, Duyn JH. Application of sensitivity-encoded echo-planar imaging for blood oxygen level-dependent functional brain imaging. Magnetic Resonance in Medicine. 2002; 48(6):1011–20. PMID: **12465111**. [PubMed: 12465111]
47. Griswold MA, Jakob PM, Edelman RR, Sodickson DK. Alternative EPI acquisition strategies using SMASH. Proc Intl Soc Mag Reson Med. 1998; 6:423.
48. Keil B, Triantafyllou C, Hamm M, Wald LL. Design optimization of a 32-channel head coil at 7T. Proc Intl Soc Mag Reson Med. 2010; 18:1493.
49. Chronik BA, Rutt BK. A comparison between human magnetostimulation thresholds in whole-body and head/neck gradient coils. Magnetic Resonance in Medicine. 2001; 46(2):386–94. PMID: **11477644**. [PubMed: 11477644]
50. Feinberg DA, Setsompop K. Ultra-fast MRI of the human brain with simultaneous multi-slice imaging. Journal of Magnetic Resonance. 2013; 229:90–100. PMID: **23473893**. [PubMed: 23473893]
51. Uğurbil K, Xu J, Auerbach EJ, Moeller S, Vu AT, Duarte-Carvajalino JM, Lenglet C, Wu X, Schmitter S, Van de Moortele P-F, Strupp J, Sapiro G, De Martino F, Wang D, Harel N, Garwood M, Chen L, et al. Pushing spatial and temporal resolution for functional and diffusion MRI in the Human Connectome Project. NeuroImage. 2013; 80:80–104. PMID: **23702417**. [PubMed: 23702417]
52. Setsompop K, Kimmlingen R, Eberlein E, Witzel T, Cohen-Adad J, McNab JA, Keil B, Tisdall MD, Hoecht P, Dietz P, Cauley SF, Tountcheva V, Matschl V, Lenz VH, Heberlein K, Potthast A, Thein H, et al. Pushing the limits of in vivo diffusion MRI for the Human Connectome Project. NeuroImage. 2013; 80:220–33. PMID: **23707579**. [PubMed: 23707579]
53. Nunes RG, Hajnal JV, Golay X, Larkman DJ. Simultaneous slice excitation and reconstruction for single shot EPI. Proc Intl Soc Mag Reson Med. 2006; 14:293.
54. Moeller S, Yacoub E, Olman CA, Auerbach EJ, Strupp J, Harel N, Uğurbil K. Multiband multislice GE-EPI at 7 tesla, with 16-fold acceleration using partial parallel imaging with application to high spatial and temporal whole-brain fMRI. Magnetic Resonance in Medicine. 2010; 63(5):1144–53. PMID: **20432285**. [PubMed: 20432285]
55. Keil B, Blau JN, Biber S, Hoecht P, Tountcheva V, Setsompop K, Triantafyllou C, Wald LL. A 64-channel 3T array coil for accelerated brain MRI. Magnetic Resonance in Medicine. 2013; 70(1): 248–58. PMID: **22851312**. [PubMed: 22851312]
56. Griffanti L, Salimi-Khorshidi G, Beckmann CF, Auerbach EJ, Douaud G, Sexton CE, Zsoldos E, Ebmeier KP, Filippini N, Mackay CE, Moeller S, Xu J, Yacoub E, Baselli G, Ugurbil K, Miller

KL, Smith SM. ICA-based artefact removal and accelerated fMRI acquisition for improved resting state network imaging. NeuroImage. 2014; 95:232–247. PMID: **24657355**. [PubMed: 24657355]

57. Chen L, Vu AT, Xu J, Moeller S, Uğurbil K, Yacoub E, Feinberg DA. Evaluation of Highly Accelerated Simultaneous Multi-Slice EPI for FMRI. NeuroImage. 2014:4–11.
58. Blaimer M, Breuer FA, Seiberlich N, Mueller MF, Heidemann RM, Jellus V, Wiggins GC, Wald LL, Griswold MA, Jakob PM. Accelerated volumetric MRI with a SENSE/GRAPPA combination. Journal of Magnetic Resonance Imaging. 2006; 24(2):444–50. PMID: **16786571**. [PubMed: 16786571]
59. Stäb D, Ritter CO, Breuer FA, Weng AM, Hahn D, Köstler H. CAIPIRINHA accelerated SSFP imaging. Magnetic Resonance in Medicine. 2011; 65:157–164. PMID: **20872868**. [PubMed: 20872868]
60. Blaimer M, Choli M, Jakob PM, Griswold MA, Breuer FA. Multiband phase-constrained parallel MRI. Magnetic Resonance in Medicine. 2013; 69(4):974–80. MID: **23440994**. [PubMed: 23440994]
61. Moeller S, Vu AT, Auerbach E, Ugurbil K, Yacoub E. RO extended FOV SENSE/GRAPPA for multiband imaging with FOV shift. Proc Intl Soc Mag Reson Med. 2014; 22:4396.
62. Cauley SF, Polimeni JR, Bhat H, Wald LL, Setsompop K. Interslice leakage artifact reduction technique for simultaneous multislice acquisitions. Magnetic Resonance in Medicine. 2014; 72(1): 93–102. PMID: **23963964**. [PubMed: 23963964]
63. Xu J, Moeller S, Auerbach EJ, Strupp J, Smith SM, Feinberg DA, Yacoub E, Uğurbil K. Evaluation of slice accelerations using multiband echo planar imaging at 3T. NeuroImage. 2013; 83:991–1001. PMID: **23899722**. [PubMed: 23899722]
64. Zhu K, Kerr A, Pauly JM. Autocalibrating CAIPIRINHA: reformulating CAIPIRINHA as a 3D problem. Proc Intl Soc Mag Reson Med. 2012; 20:518.
65. Riemenschneider B, Assländer J, Hennig J. An approach to 3-dimensional multi-band acquisition. Proc Intl Soc Mag Reson Med. 2013; 21:401.
66. Zahneisen B, Ernst T, Poser BA. SENSE and simultaneous multislice imaging. Magnetic Resonance in Medicine. 2015; 74(5):1356–1362. PMID: **25376715**. [PubMed: 25376715]
67. Zhang T, Pauly JM, Vasanawala SS, Lustig M. Coil compression for accelerated imaging with Cartesian sampling. Magnetic Resonance in Medicine. 2013; 69(2):571–82. PMID: **22488589**. [PubMed: 22488589]
68. Cauley S, Lustig M, Bilgic B, Bhat H, Wald LL, Setsompop K. Geometric-decomposition coil compression for real-time Simultaneous MultiSlice EPI reconstruction at high MultiBand factors. Proc Intl Soc Mag Reson Med. 2014; 22:4404.
69. Polimeni JR, Bhat H, Witzel T, Benner T, Feiweier T, Inati SJ, Renvall V, Heberlein K, Wald LL. Reducing sensitivity losses due to respiration and motion in accelerated echo planar imaging by reordering the autocalibration data acquisition. Magnetic Resonance in Medicine. 2016; 75(2): 665–679. PMID: **25809559**. [PubMed: 25809559]
70. Griswold MA, Breuer F, Blaimer M, Kannengiesser S, Heidemann RM, Mueller M, Nittka M, Jellus V, Kiefer B, Jakob PM. Autocalibrated coil sensitivity estimation for parallel imaging. NMR in Biomedicine. 2006; 19(3):316–24. PMID: **16705632**. [PubMed: 16705632]
71. Talagala SL, Sarlls JE, Inati SJ. Improved temporal SNR of accelerated EPI using a FLASH based GRAPPA reference scan. Proc Intl Soc Mag Reson Med. 2013; 21:2658.
72. Talagala SL, Sarlls JE, Inati SJ. Improved temporal SNR of accelerated EPI using a FLASH based GRAPPA reference scan. Proceedings of the International Society for Magnetic Resonance in Medicine. 2013; 21:2658.
73. Vu AT, Moeller S, Auerbach EJ, Uğurbil K, Yacoub E. GRE reference scan for robust reconstruction of high resolution slice and in-plane accelerated 2D GE EPI at 7T. Proc Intl Soc Mag Reson Med. 2014; 22:1414.
74. Chapman B, Turner R, Ordidge RJ, Doyle M, Cawley M, Coxon R, Glover P, Mansfield P. Real-time movie imaging from a single cardiac cycle by NMR. Magnetic Resonance in Medicine. 1987; 5(3):246–54. PMID: **3431393**. [PubMed: 3431393]
75. Mansfield P. Spatial mapping of the chemical shift in NMR. Magnetic Resonance in Medicine. 1984; 1(3):370–86. PMID: **6571566**. [PubMed: 6571566]

76. Guilfoyle DN, Hrabe J. Interleaved snapshot echo planar imaging of mouse brain at 7.0 T. NMR in Biomedicine. 2006; 19(1):108–15. PMID: **16411168**. [PubMed: 16411168]
77. Kang D, Chung J, Kim D, Kim Y, Cho Z-H. A modified variable flip angle using a predefiend slice profile in a consecutive interleaved EPI. Proc Intl Soc Mag Reson Med. 2012; 20:2453.
78. Bhat H, Polimeni JR, Cauley SF, Setsompop K, Wald LL, Heberlein K. Motion Insensitive ACS Acquisition Method for in-plane and Simultaneous Multi-Slice Accelerated EPI. Proc Intl Soc Mag Reson Med. 2014; 22:644.
79. Wiesinger F, Van de Moortele P-F, Adriany G, De Zanche N, Ugurbil K, Pruessmann KP. Parallel imaging performance as a function of field strength--an experimental investigation using electrodynamic scaling. Magnetic Resonance in Medicine. 2004; 52(5):953–64. PMID: **15508167**. [PubMed: 15508167]
80. Chu A, Noll DC. Simultaneous multislice spiral imaging using z-gradient modulation and parallel receive coils. Proc Intl Soc Mag Reson Med. 2013; 62(2):3317.
81. Zahneisen B, Poser BA, Ernst T, Stenger VA. Blipped-CAIPI Spiral for Simultaneous Multi-Slice BOLD fMRI. Proc Intl Soc Mag Reson Med. 2013; 21:409.
82. Zahneisen B, Poser BA, Ernst T, Stenger AV. Simultaneous Multi-Slice fMRI using spiral trajectories. NeuroImage. 2014; 92:8–18. PMID: **24518259**. [PubMed: 24518259]
83. Butts K, Riederer SJ, Ehman RL, Thompson RM, Jack CR. Interleaved echo planar imaging on a standard MRI system. Magnetic Resonance in Medicine. 1994; 31(1):67–72. PMID: **8121272**. [PubMed: 8121272]
84. Polimeni JR, Setsompop K, Gagoski BA, McNab JA, Triantafyllou C, Wald LL. Rapid multi-shot segmented EPI using the Simultaneous Multi-Slice acquisition method. Proc Intl Soc Mag Reson Med. 2012; 20:2222.
85. Melcher, JR., Setsompop, K., Knudson, IM., Levine, RA. Whole-brain fMRI without increased scanner-generated acoustic noise: application to tinnitus. 1The 34th Annual Midwinter Research Meeting of the Association for Research in Otolaryngology (ARO), Baltimore; Feb 19–23. 2011 p. 532011abstract 156
86. De Martino F, Moerel M, Ugurbil K, Formisano E, Yacoub E. Less noise, more activation: Multiband acquisition schemes for auditory functional MRI. Magnetic Resonance in Medicine. 2015; 74(2):462–7. PMID: **25105832**. [PubMed: 25105832]
87. Olafsson V, Guo J, Wong CW, Kundu P, Inati SJ, Luh W-M, Roopchansingh V, Brenowitz N, Bandettini PA, Wong E, Liu T. High spatial and temporal resolution fcMRI with BOLD selectivity using multiecho simultaneous multislice EPI. Proc Intl Soc Mag Reson Med. 2012; 20:2068.
88. Boyacioglu R, Schulz J, Koopmans P, Barth M, Norris D. Improving sensitivity and specificity for rs-EPI using Multiband Multi-Echo EPI at 7T. Proc Intl Soc Mag Reson Med. 2014; 22:1502.
89. Poser BA, Koopmans PJ, Witzel T, Wald LL, Barth M. Three dimensional echo-planar imaging at 7 Tesla. NeuroImage. 2010; 51(1):261–6. PMID: **20139009**. [PubMed: 20139009]
90. van der Zwaag W, Marques JP, Kober T, Glover G, Gruetter R, Krueger G. Temporal SNR Characteristics in Segmented 3D-EPI at 7T. Magnetic Resonance in Medicine. 2012; 67(2):344–352. [PubMed: 21656557]
91. Poser BA, Ivanov D, Kannengiesser SA, Uludag K, Barth M. Accelerated 3D EPI using 2D blipped-CAIPI for high temporal and/or spatial resolution. Proc Intl Soc Mag Reson Med. 2014; 22:1506.
92. Narsude M, Gallichan D, van der Zwaag W, Gruetter R, Marques J. Whole brain fMRI in 370ms: exploring the benefits of high temporal resolution 3D-EPI-CAIPI. Proc Intl Soc Mag Reson Med. 2014; 67(2):643.
93. Lutti A, Thomas DL, Hutton C, Weiskopf N. High-resolution functional MRI at 3 T: 3D/2D echo-planar imaging with optimized physiological noise correction. Magnetic Resonance in Medicine. 2013; 69(6):1657–64. PMID: **22821858**. [PubMed: 22821858]
94. Afacan O, Hoge WS, Janoos F, Brooks DH, Morocz IA. Rapid full-brain fMRI with an accelerated multi shot 3D EPI sequence using both UNFOLD and GRAPPA. Magnetic Resonance in Medicine. 2012; 67(5):1266–74. PMID: **22095768**. [PubMed: 22095768]

95. Narsude M, van der Zwaag W, Kober T, Gruetter R, Marques JP. Improved temporal resolution for functional studies with reduced number of segments with three-dimensional echo planar imaging. Magnetic Resonance in Medicine. 2014; 72(3):786–92. PMID: **24136782**. [PubMed: 24136782]

96. Hu Y, Glover GH. Three-dimensional spiral technique for high-resolution functional MRI. Magnetic Resonance in Medicine. 2007; 58:947–51. PMID: **17969117**. [PubMed: 17969117]

97. Deng W, Zahneisen B, Stenger VA. Stack-of-Spirals CAIPIRINHA Trajectory for Rapid Volumetric Imaging. Proc Intl Soc Mag Reson Med. 2014; 22(1):642.

98. Feinberg A, Hoenninger JC, Crooks LE, Kaufman L, Watts JC, Arakawa M. Inner volume MR imaging: technical concepts and their application. Radiology. 1985; 156:743–747. [PubMed: 4023236]

99. Feinberg DA, Hale JS. Echo planar-inner volume imaging at 0.35T. Proc Soc Mag Reson Med. 1986; 5:950.

100. Mansfield P, Ordidge RJ, Coxon R. Zonally magnified EPI in real time by NMR. Journal of Physics E: Scientific Instruments. 1988; 21(3):275–280.

101. Luo Y, de Graaf RA, Delabarre L, Tannús A, Garwood M. BISTRO: An outer-volume suppression method that tolerates RF field inhomogeneity. Magnetic Resonance in Medicine. 2001; 45(6):1095–1102. PMID: **11378888**. [PubMed: 11378888]

102. Pfeuffer J, Van de Moortele P-F, Yacoub E, Shmuel A, Adriany G, Andersen P, Merkle H, Garwood M, Uğurbil K, Hu X. Zoomed Functional Imaging in the Human Brain at 7 Tesla with Simultaneous High Spatial and High Temporal Resolution. NeuroImage. 2002; 17(1):272–286. [PubMed: 12482083]

103. Wargo CJ, Gore JC. Rapid high resolution 3D volume imaging of the human brain using spin echo EPI, parallel imaging, reduced-FOV methods, and oversampling reduction at 7T. Proc Intl Soc Mag Reson Med. 2013; 21:2363.

104. Heidemann RM, Ivanov D, Trampel R, Fasano F, Meyer H, Pfeuffer J, Turner R. Isotropic submillimeter fMRI in the human brain at 7 T: combining reduced field-of-view imaging and partially parallel acquisitions. Magnetic Resonance in Medicine. 2012; 68(5):1506–16. PMID: **22231859**. [PubMed: 22231859]

105. Feinberg DA, Chen L, Vu AT. Zoomed resolution in Simultaneous Multi-Slice EPI for fMRI. Proc Intl Soc Mag Reson Med. 2013; 21:3316.

106. Finsterbusch J. Simultaneous functional MRI acquisition of distributed brain regions with high temporal resolution using a 2D-selective radiofrequency excitation. Magnetic Resonance in Medicine. 2015; 73(2):683–91. PMID: **24574142**. [PubMed: 24574142]

107. Boxerman JL, Bandettini PA, Kwong KK, Baker JR, Davis TL, Rosen BR, Weisskoff RM. The intravascular contribution to fMRI signal change: Monte Carlo modeling and diffusion-weighted studies in vivo. Magnetic Resonance in Medicine. 1995; 34(1):4–10. PMID: **7674897**. [PubMed: 7674897]

108. Uludağ K, Müller-Bierl B, Uğurbil K. An integrative model for neuronal activity-induced signal changes for gradient and spin echo functional imaging. NeuroImage. 2009; 48(1):150–65. PMID: **19481163**. [PubMed: 19481163]

109. Ogawa S, Menon R, Tank D, Kim S, Merkle H, Ellermann J, Ugurbil K. Functional brain mapping by blood oxygenation level-dependent contrast magnetic resonance imaging. A comparison of signal characteristics with a biophysical model. Biophysical Journal. 1993; 64(3): 803–812. [PubMed: 8386018]

110. Oshio K, Feinberg DA. GRASE (Gradient- and spin-echo) imaging: a novel fast MRI technique. Magnetic Resonance in Medicine. 1991; 20(2):344–9. PMID: **1775061**. [PubMed: 1775061]

111. Feinberg DA, Harel N, Ramanna S, Uğurbil K, Yacoub E. Sub-millimeter single-shot 3D GRASE with inner volume selection for T2-weighted fMRI applications at 7 Tesla. Proc Intl Soc Mag Reson Med. 2008; 16:2373.

112. Zimmermann J, Goebel R, De Martino F, Van de Moortele P-F, Feinberg DA, Adriany G, Chaimow D, Shmuel A, Uğurbil K, Yacoub E. Mapping the organization of axis of motion selective features in human area MT using high-field fMRI. PloS one. 2011; 6(12):e28716. PMID: **22163328**. [PubMed: 22163328]

113. De Martino F, Zimmermann J, Muckli L, Uğurbil K, Yacoub E, Goebel R. Cortical depth dependent functional responses in humans at 7T: improved specificity with 3D GRASE. PloS one. 2013; 8(3):e60514. [PubMed: 23533682]
114. Chen L, Feinberg DA. Simultaneous Multi-Volume GRASE Imaging. Proc Intl Soc Mag Reson Med. 2013; 21:2365.
115. Vu AT, Feinberg DA, Harel N, Uğurbil K, Yacoub ES. Diagonal multi-slab inner volume 3D GRASE imaging for high resolution T2 weighted fMRI. Proc Intl Soc Mag Reson Med. 2013; 21:2364.
116. Kemper VG, De Martino F, Vu AT, Feinberg DA, Yacoub E, Goebel R. Variable Flip Angle 3D-GRASE for increased spatial coverage and improved point spread function in high hesolution fMRI at 7T. Proc Intl Soc Mag Reson Med. 2014; 22:2986.
117. Chen L, Feinberg DA. Simultaneous Multi-Slab Echo Volume Imaging: comparison in sub-second fMRI. Proc Intl Soc Mag Reson Med. 2013; 21:303.
118. Ghariq E, Teeuwisse WM, Webb AG, van Osch MJP. Feasibility of pseudocontinuous arterial spin labeling at 7 T with whole-brain coverage. Magn Reson Mater Phy. 2012; 25:83–93. PMID: **22200964**.
119. Zuo Z, Wang R, Zhuo Y, Xue R, St Lawrence KS, Wang DJJ. Turbo-FLASH based arterial spin labeled perfusion MRI at 7 T. PloS one. 2013; 8(6):e66612. PMID: **23818950**. [PubMed: 23818950]
120. Gardener AG, Jezzard P. Investigating white matter perfusion using optimal sampling strategy arterial spin labeling at 7 Tesla. Magnetic Resonance in Medicine. 2015; 73(6):2243–8. PMID: **24954898**. [PubMed: 24954898]
121. Luh W-M, Talagala SL, Li T-Q, Bandettini PA. Pseudo-continuous arterial spin labeling at 7 T for human brain: estimation and correction for off-resonance effects using a Prescan. Magnetic Resonance in Medicine. 2013; 69:402–10. PMID: **22488568**. [PubMed: 22488568]
122. Hare HV, Blockley NP, Gardener AG, Clare S, Bulte DP. Investigating the field-dependence of the Davis model: Calibrated fMRI at 1.5, 3 and 7T. NeuroImage. 2015; 112:189–196. PMID: **25783207**. [PubMed: 25783207]
123. Kim T, Shin W, Zhao T, Beall EB, Lowe MJ, Bae KT. Whole brain perfusion measurements using arterial spin labeling with multiband acquisition. Magnetic Resonance in Medicine. 2013; 70(6): 1653–61. PMID: **23878098**. [PubMed: 23878098]
124. Feinberg DA, Beckett A, Chen L. Arterial spin labeling with simultaneous multi-slice echo planar imaging. Magnetic Resonance in Medicine. 2013; 70(6):1500–6. PMID: **24130105**. [PubMed: 24130105]
125. Wang Y, Moeller S, Vu AT, Ugurbil K, Yacoub E, Wang DJ. Whole-brain distortion-free pseudo-continuous arterial spin labeling using multiband turbo-FLASH at 3 and 7T. Proc Intl Soc Mag Reson Med. 2014; 22:2697.
126. Li X, Wang D, Auerbach EJ, Moeller S, Ugurbil K, Metzger GJ. Theoretical and experimental evaluation of multi-band EPI for high-resolution whole brain pCASL Imaging. NeuroImage. 2015; 106:170–81. PMID: **25462690**. [PubMed: 25462690]
127. Ivanov D, Poser BA, Huber L, Pfeuffer J, Uludag K. Whole-brain Perfusion Measurements at 7T using Pulsed Arterial Spin Labelling and Simultaneous Multi-slice Multi-echo Echo Planar Imaging. Proc Intl Soc Mag Reson Med. 2014; 22:2698. PMID: **24130105**.
128. Wang D, Cantrell C, Spottiswoode B, Deshpande V, Carroll T, Heberlein K. Slice accelerated EPI for Dynamic-Susceptibility Contrast enhanced (DSC) MRI. Proc Intl Soc Mag Reson Med. 2013; 21:584.
129. Eichner C, Jafari-Khouzani K, Cauley S, Bhat H, Polaskova P, Andronesi OC, Rapalino O, Turner R, Wald LL, Stufflebeam S, Setsompop K. Slice accelerated gradient-echo spin-echo dynamic susceptibility contrast imaging with blipped CAIPI for increased slice coverage. Magnetic Resonance in Medicine. 2014; 72(3):770–8. PMID: **24285593**. [PubMed: 24285593]
130. Knutsson L, Ståhlberg F, Wirestam R. Aspects on the accuracy of cerebral perfusion parameters obtained by dynamic susceptibility contrast MRI: a simulation study. Magnetic Resonance Imaging. 2004; 22(6)):789–98. PMID: **15234447**. [PubMed: 15234447]

131. Sotiropoulos SN, Jbabdi S, Xu J, Andersson JL, Moeller S, Auerbach EJ, Glasser MF, Hernandez M, Sapiro G, Jenkinson M, Feinberg DA, Yacoub E, Lenglet C, Essen D. C. Van, Uğurbil K, Behrens TEJ, Hcp W. Advances in diffusion MRI acquisition and processing in the Human Connectome Project. NeuroImage. 2013; 80:125–143. [PubMed: 23702418]

132. Vu AT, Auerbach EJ, Lenglet C, Moeller S, Sein J, Van de Moortele P-F, Uğurbil K, Yacoub E. High resolution whole brain diffusion imagining at 7T for the Human Connectome Project. Proc Intl Soc Mag Reson Med. 2014; 22:1000.

133. Mukherjee P, Hess CP, Xu D, Han ET, Kelley DA, Vigneron DB. Development and initial evaluation of 7-T q-ball imaging of the human brain. Magnetic Resonance Imaging. 2008; 26(2): 171–80. PMID: **17692489**. [PubMed: 17692489]

134. Poupon C, Wiggins CJ, Descoteaux M, Feiweier T, Mangin J-F, Le Bihan D. Millimeter analytical Q-ball fiber density function for a better separation of fiber populations at 7T. Proc Intl Soc Mag Reson Med. 2009; 17:1400.

135. Bammer R, Keeling SL, Augustin M, Pruessmann KP, Wolf R, Stollberger R, Hartung H, Fazekas F. Improved diffusion-weighted single-shot Echo-Planar Imaging (EPI) in stroke using sensitivity encoding (SENSE). Magnetic Resonance in Medicine. 2001; 46:548–554. [PubMed: 11550248]

136. Jaermann T, Crelier G, Pruessmann KP, Golay X, Netsch T, van Muiswinkel AM, Mori S, van Zijl PCM, Valavanis A, Kollias S, Boesiger P. SENSE-DTI at 3 T. Magnetic Resonance in Medicine. 2004; 51(2):230–6. PMID: **14755645**. [PubMed: 14755645]

137. Reischauer C, Vorburger RS, Wilm BJ, Jaermann T, Boesiger P. Optimizing signal-to-noise ratio of high-resolution parallel single-shot diffusion-weighted echo-planar imaging at ultrahigh field strengths. Magnetic Resonance in Medicine. 2012; 67(3):679–90. PMID: **21702067**. [PubMed: 21702067]

138. Setsompop K, Cohen-Adad J, Gagoski BA, Raij T, Yendiki A, Keil B, Wedeen VJ, Wald LL. Improving diffusion MRI using simultaneous multi-slice echo planar imaging. NeuroImage. 2012; 63(1):569–80. PMID: **22732564**. [PubMed: 22732564]

139. Wargo CJ, Moore J, Gore JC. A comparison and evaluation of reduced-FOV methods for multi-slice 7 T human imaging. Magnetic Resonance Imaging. 2013; 31:1349–1359. [PubMed: 23891434]

140. von Morze C, Kelley DAC, Shepherd TM, Banerjee S, Xu D, Hess CP. Reduced field-of-view diffusion-weighted imaging of the brain at 7 T. Magnetic Resonance Imaging. 2010; 28(10): 1541–5. PMID: **20850242**. [PubMed: 20850242]

141. Heidemann RM, Anwander A, Feiweier T, Knösche TR, Turner R. k-space and q-space: combining ultra-high spatial and angular resolution in diffusion imaging using ZOOPPA at 7 T. NeuroImage. 2012; 60(2):967–78. PMID: **22245337**. [PubMed: 22245337]

142. Wargo CJ, Gore JC. Localized high-resolution DTI of the human midbrain using single-shot EPI, parallel imaging, and outer-volume suppression at 7 T. Magnetic Resonance Imaging. 2013; 31:810–819. [PubMed: 23541390]

143. Bianciardi M, Toschi N, Edlow BL, Eichner C, Setsompop K, Polimeni JR, Brown EN, Kinney HC, Rosen BR, Wald LL. Toward an In Vivo Neuroimaging Template of Human Brainstem Nuclei of the Ascending Arousal, Autonomic, and Motor Systems. Brain Connectivity. 2015; 5(10):597–607. PMID: **26066023**. [PubMed: 26066023]

144. Saritas EU, Lee D, Cukur T, Shankaranarayanan A, Nishimura DG. Hadamard slice encoding for reduced-FOV diffusion-weighted imaging. Magnetic resonance in Medicine. 2014; 72(5):1277–90. PMID: **24265013**. [PubMed: 24265013]

145. Eichner C, Setsompop K, Koopmans PJ, Lützkendorf R, Norris DG, Turner R, Wald LL, Heidemann RM. Slice accelerated diffusion-weighted imaging at ultra-high field strength. Magnetic Resonance in Medicine. 2014; 71(4):1518–25. PMID: **23798017**. [PubMed: 23798017]

146. Norris DG, Koopmans PJ, Boyacioğlu R, Barth M. Power Independent of Number of Slices (PINS) radiofrequency pulses for low-power simultaneous multislice excitation. Magnetic Resonance in Medicine. 2011; 66(5):1234–40. PMID: **22009706**. [PubMed: 22009706]

147. Porter DA, Mueller E. Multi-shot diffusion-weighted EPI with readout mosaic segmentation and 2D navigator correction. Proc Intl Soc Mag Reson Med. 2004; 12:442.

148. Holdsworth SJ, Skare S, Newbould RD, Guzmann R, Blevins NH, Bammer R. Readout-segmented EPI for rapid high resolution diffusion imaging at 3 T. European Journal of Radiology. 2008; 65(1):36–46. PMID: **17980534**. [PubMed: 17980534]

149. Porter DA, Heidemann RM. High resolution diffusion-weighted imaging using readout-segmented echo-planar imaging, parallel imaging and a two-dimensional navigator-based reacquisition. Magnetic Resonance in Medicine. 2009; 62(2):468–75. PMID: **19449372**. [PubMed: 19449372]

150. Heidemann RM, Porter DA, Anwander A, Feiweier T, Heberlein K, Knösche TR, Turner R. Diffusion imaging in humans at 7T using readout-segmented EPI and GRAPPA. Magnetic Resonance in Medicine. 2010; 64(1):9–14. PMID: **20577977**. [PubMed: 20577977]

151. Frost R, Porter DA, Miller KL, Jezzard P. Implementation and assessment of diffusion-weighted partial Fourier readout-segmented echo-planar imaging. Magnetic Resonance in Medicine. 2012; 68(2):441–51. PMID: **22535706**. [PubMed: 22535706]

152. Frost R, Jezzard P, Douaud G, Clare S, Porter DA, Miller KL, Miller KL. Scan time reduction for readout-segmented EPI using simultaneous multislice acceleration: Diffusion-weighted imaging at 3 and 7 Tesla. Magnetic Resonance in Medicine. 2015; 74:136–149. PMID: **25078777**.

153. Peterson E, Holdsworth SJ, O'Halloran R, Aboussouan E, Bammer R. Readout-Segmented Diffusion Tensor Imaging (RS-DTI) acceleration using simultaneously acquired slices. Proc Intl Soc Mag Reson Med. 2014; 62(6):2560.

154. Jeong H-K, Gore JC, Anderson AW. High-resolution human diffusion tensor imaging using 2-D navigated multishot SENSE EPI at 7 T. Magnetic Resonance in Medicine. 2013; 69(3):793–802. PMID: **22592941**. [PubMed: 22592941]

155. Chen N, Guidon A, Chang H, Song AW. A robust multi-shot scan strategy for high-resolution diffusion weighted MRI enabled by multiplexed sensitivity-encoding (MUSE). NeuroImage. 2013; 72:41–47. [PubMed: 23370063]

156. Chang H-C, Guhaniyogi S, Chen N-K. Interleaved diffusion-weighted improved by adaptive partial-Fourier and multiband multiplexed sensitivity-encoding reconstruction. Magnetic Resonance in Medicine. 2014 In press. PMID: **24925000**.

157. Menzel MI, Tan ET, Khare K, Sperl JI, King KF, Tao X, Hardy CJ, Marinelli L. Accelerated diffusion spectrum imaging in the human brain using compressed sensing. Magnetic Resonance in Medicine. 2011; 66(5):1226–33. PMID: **22012686**. [PubMed: 22012686]

158. Bilgic B, Setsompop K, Cohen-Adad J, Yendiki A, Wald LL, Adalsteinsson E. Accelerated diffusion spectrum imaging with compressed sensing using adaptive dictionaries. Magnetic Resonance in Medicine. 2012; 68(6):1747–54. PMID: **23008145**. [PubMed: 23008145]

159. Gramfort A, Poupon C, Descoteaux M. Sparse DSI: Learning DSI Structure for Denoising and Fast Imaging. Medical image computing and computer-assisted interventio. 2012; 15(Part2):288–296.

160. Merlet S, Caruyer E, Deriche R. Parametric dictionary learning for modeling EAP and ODF in diffusion MRI. Medical image computing and computer-assisted intervention. 2012; 15:10–17.

161. Rathi Y, Michailovich O, Setsompop K, Bouix S, Shenton ME, Westin C-F. Sparse multi-shell diffusion imaging. Medical image computing and computer-assisted intervention. 2011; 14(2): 58–65.

162. Duarte-Carvajalino JM, Lenglet C, Xu J, Yacoub E, Uğurbil K, Moeller S, Carin L, Sapiro G. Estimation of the CSA-ODF using Bayesian compressed sensing of multi-shell HARDI. Magnetic Resonance in Medicine. 2014; 72:1471–1485. PMID: **24338816**. [PubMed: 24338816]

163. Setsompop K, Bilgic B, Cohen-adad J, Tisdall MD, Keil B, Witzel T, Rathi Y, Wedeen VJ, Adalsteinsson E, Wald LL. Whole-brain DSI in 4 minutes: sparse sampling in q-space with simultaneous multi-slice acquisition. Proc Intl Soc Mag Reson Med. 2012; 20:693.

164. Cho Z-H, Kang C-K, Han J-Y, Kim S-H, Kim K-N, Hong S-M, Park C-W, Kim Y-B. Observation of the lenticulostriate arteries in the human brain in vivo using 7.0T MR angiography. Stroke. 2008; 39(5):1604–6. PMID: **18340096**. [PubMed: 18340096]

165. Lüsebrink F, Wollrab A, Speck O. Cortical thickness determination of the human brain using high resolution 3T and 7T MRI data. NeuroImage. 2013; 70:122–31. PMID: **23261638**. [PubMed: 23261638]

166. Geyer S, Weiss M, Reimann K, Lohmann G, Turner R. Microstructural parcellation of the human cerebral cortex - from Brodmann's post-mortem map to in vivo mapping with high-field Magnetic Resonance Imaging. Frontiers in Human Neuroscience. 2011; 5:19. PMID: **21373360**. [PubMed: 21373360]

167. De Martino F, Moerel M, Xu J, van de Moortele P-F, Ugurbil K, Goebel R, Yacoub E, Formisano E. High-Resolution Mapping of Myeloarchitecture In Vivo: Localization of Auditory Areas in the Human Brain. Cerebral Cortex. 2015; 25(10):3394–405. PMID: **24994817**. [PubMed: 24994817]

168. Clare S, Bridge H. Methodological issues relating to in vivo cortical myelography using MRI. Human Brain Mapping. 2005; 26(4):240–50. PMID: **15954140**. [PubMed: 15954140]

169. Tourdias T, Saranathan M, Levesque IR, Su J, Rutt BK. Visualization of intra-thalamic nuclei with optimized white-matter-nulled MPRAGE at 7T. NeuroImage. 2014; 84:534–45. PMID: **24018302**. [PubMed: 24018302]

170. Keuken MC, Bazin P-L, Crown L, Hootsmans J, Laufer A, Müller-Axt C, Sier R, van der Putten EJ, Schäfer A, Turner R, Forstmann BU. Quantifying inter-individual anatomical variability in the subcortex using 7 T structural MRI. NeuroImage. 2014; 94:40–6. PMID: **24650599**. [PubMed: 24650599]

171. Norris DG, Boyacioğlu R, Schulz J, Barth M, Koopmans PJ. Application of PINS radiofrequency pulses to reduce power deposition in RARE/turbo spin echo imaging of the human head. Magnetic Resonance in Medicine. 2014; 71(1):44–9. PMID: **24150771**. [PubMed: 24150771]

172. Mugler JP, Brookeman JR. Three-dimensional magnetization-prepared rapid gradient-echo imaging (3D MP RAGE). Magnetic Resonance in Medicine. 1990; 15(1):152–7. PMID: **2374495**. [PubMed: 2374495]

173. Mugler JP, Epstein FH, Brookeman JR. Shaping the signal response during the approach to steady state in three-dimensional magnetization-prepared rapid gradient-echo imaging using variable flip angles. Magnetic Resonance in Medicine. 1992; 28(2):165–85. PMID: **1461121**. [PubMed: 1461121]

174. Visser F, Zwanenburg JJM, Hoogduin JM, Luijten PR. High-resolution magnetization-prepared 3D-FLAIR imaging at 7.0 Tesla. Magnetic Resonance in Medicine. 2010; 64(1):194–202. PMID: **20572143**. [PubMed: 20572143]

175. Tisdall MD, Polimeni JR, van der Kouwe AJW. Motion-corrected 350 μm isotropic MPRAGE at 3 T using volumetric navigators (vNavs). Proc Intl Soc Mag Reson Med. 2013; 21:268.

176. van der Kouwe AJW, Tisdall MD, Bhat H, Fischl B, Polimeni JR. Multiple echo and inversion time MPRAGE with Inner Loop GRAPPA acceleration and prospective motion correction for minimally distorted multispectral brain morphometry. Proc Intl Soc Mag Reson Med. 2014; 22:120.

177. van der Kouwe AJW, Benner T, Salat DH, Fischl B. Brain morphometry with multiecho MPRAGE. NeuroImage. 2008; 40(2):559–69. PMID: **18242102**. [PubMed: 18242102]

178. Marques JP, Kober T, Krueger G, van der Zwaag W, Van de Moortele P-F, Gruetter R. MP2RAGE, a self bias-field corrected sequence for improved segmentation and T1-mapping at high field. NeuroImage. 2010; 49(2):1271–81. PMID: **19819338**. [PubMed: 19819338]

179. Haacke EM, Xu Y, Cheng Y-CN, Reichenbach JR. Susceptibility weighted imaging (SWI). Magnetic Resonance in Medicine. 2004; 52(3):612–8. PMID: **15334582**. [PubMed: 15334582]

180. Deistung A, Rauscher A, Sedlacik J, Stadler J, Witoszynskyj S, Reichenbach JR. Susceptibility weighted imaging at ultra high magnetic field strengths: theoretical considerations and experimental results. Magnetic Resonance in Medicine. 2008; 60(5):1155–68. PMID: **18956467**. [PubMed: 18956467]

181. de Rochefort L, Liu T, Kressler B, Liu J, Spincemaille P, Lebon V, Wu J, Wang Y. Quantitative susceptibility map reconstruction from MR phase data using bayesian regularization: validation and application to brain imaging. Magnetic Resonance in Medicine. 2010; 63(1):194–206. PMID: **19953507**. [PubMed: 19953507]

182. Shmueli K, Zwart J. De. Magnetic susceptibility mapping of brain tissue in vivo using MRI phase data. Magnetic Resonance in Medicine. 2009; 62:1510–1. [PubMed: 19859937]

183. Marques JP, Bowtell R. Application of a Fourier-based method for rapid calculation of field inhomogeneity due to spatial variation of magnetic susceptibility. Concepts in Magnetic Resonance Part B: Magnetic Resonance Engineering. 2005; 25B(1):65–78.

184. Liu T, Liu J, de Rochefort L, Spincemaille P, Khalidov I, Ledoux JR, Wang Y. Morphology enabled dipole inversion (MEDI) from a single-angle acquisition: comparison with COSMOS in human brain imaging. Magnetic Resonance in Medicine. 2011; 66(3):777–83. PMID: **21465541**. [PubMed: 21465541]

185. Bilgic B, Pfefferbaum A, Rohlfing T, Sullivan EV, Adalsteinsson E. MRI estimates of brain iron concentration in normal aging using quantitative susceptibility mapping. NeuroImage. 2012; 59(3):2625–35. PMID: **21925274**. [PubMed: 21925274]

186. Liu T, Spincemaille P, de Rochefort L, Kressler B, Wang Y. Calculation of susceptibility through multiple orientation sampling (COSMOS): a method for conditioning the inverse problem from measured magnetic field map to susceptibility source image in MRI. Magnetic Resonance in Medicine. 2009; 61(1):196–204. PMID: **19097205**. [PubMed: 19097205]

187. Deistung A, Schäfer A, Schweser F, Biedermann U, Turner R, Reichenbach JR. Toward in vivo histology: a comparison of quantitative susceptibility mapping (QSM) with magnitude-, phase-, and R2*-imaging at ultra-high magnetic field strength. NeuroImage. 2013; 65:299–314. [PubMed: 23036448]

188. Wharton S, Bowtell R. Whole-brain susceptibility mapping at high field: a comparison of multiple-and single-orientation methods. Neuroimage. 2010; 53(2):515–525. [PubMed: 20615474]

189. Li W, Wu B, Avram AV, Liu C. Magnetic susceptibility anisotropy of human brain in vivo and its molecular underpinnings. NeuroImage. 2012; 59(3):2088–97. PMID: **22036681**. [PubMed: 22036681]

190. Liu C. Susceptibility tensor imaging. Magnetic Resonance in Medicine. 2010; 63(6):1471–1477. [PubMed: 20512849]

191. Wisnieff C, Liu T, Spincemaille P, Wang S, Zhou D, Wang Y. Magnetic susceptibility anisotropy: cylindrical symmetry from macroscopically ordered anisotropic molecules and accuracy of MRI measurements using few orientations. NeuroImage. 2013; 70:363–76. PMID: **23296181**. [PubMed: 23296181]

192. Li X, Vikram DS, Lim IAL, Jones CK, Farrell J. a D. van Zijl PCM. Mapping magnetic susceptibility anisotropies of white matter in vivo in the human brain at 7 T. NeuroImage. 2012; 62(1):314–30. PMID: **22561358**. [PubMed: 22561358]

193. Xu Y, Haacke EM. An iterative reconstruction technique for geometric distortion-corrected segmented echo-planar imaging. Magnetic Resonance Imaging. 2008; 26(10):1406–14. PMID: **18783907**. [PubMed: 18783907]

194. Wu B, Li W, Avram AV, Gho S-M, Liu C. Fast and tissue-optimized mapping of magnetic susceptibility and T2* with multi-echo and multi-shot spirals. NeuroImage. 2012; 59(1):297–305. PMID: **21784162**. [PubMed: 21784162]

195. Skare S, Newbould RD, Clayton DB, Bammer R. Propeller EPI in the other direction. Magnetic Resonance in Medicine. 2006; 55(6):1298–307. PMID: **16676335**. [PubMed: 16676335]

196. Holdsworth SJ, Yeom KW, Moseley ME, Skare S. Fast susceptibility-weighted imaging with three-dimensional short-axis propeller (SAP)-echo-planar imaging. Journal of Magnetic Resonance Imaging. 2015; 41(5):1447–53. PMID: **24956237**. [PubMed: 24956237]

197. Zwanenburg JJM, Versluis MJ, Luijten PR, Petridou N. Fast high resolution whole brain T2* weighted imaging using echo planar imaging at 7T. NeuroImage. 2011; 56(4):1902–7. PMID: **21440070**. [PubMed: 21440070]

198. Khabipova D, Wiaux Y, Gruetter R, Marques JP. A modulated closed form solution for quantitative susceptibility mapping--a thorough evaluation and comparison to iterative methods based on edge prior knowledge. NeuroImage. 2015; 107:163–74. [PubMed: 25463463]

199. Sati P, Thomasson DM, Li N, Pham DL, Biassou NM, Reich DS, Butman JA. Rapid, high-resolution, whole-brain, susceptibility-based MRI of multiple sclerosis. Multiple Sclerosis. 2014; 20(11):1464–70. PMID: **24639479**. [PubMed: 24639479]

200. Langkammer C, Bredies K, Poser BA, Barth M, Reishofer G, Fan AP, Bilgic B, Fazekas F, Mainero C, Ropele S. Fast quantitative susceptibility mapping using 3D EPI and total generalized variation. NeuroImage. 2015; 111:622–30. [PubMed: 25731991]

201. Bilgic B, Gagoski BA, Cauley SF, Fan AP, Polimeni JR, Grant PE, Wald LL, Setsompop K. Wave-CAIPI for highly accelerated 3D imaging. Magnetic Resonance in Medicine. 2015; 73(6): 2152–62. PMID: **24986223**. [PubMed: 24986223]

202. Moriguchi H, Duerk JL. Bunched phase encoding (BPE): a new fast data acquisition method in MRI. Magnetic Resonance in Medicine. 2006; 55(3):633–48. PMID: **16470597**. [PubMed: 16470597]

203. Breuer FA, Moriguchi H, Seiberlich N, Blaimer M, Jakob PM, Duerk JL, Griswold MA. Zigzag sampling for improved parallel imaging. Magnetic Resonance in Medicine. 2008; 60(2):474–8. PMID: **18666134**. [PubMed: 18666134]

204. Breuer, F. Development and Application of Efficient Strategies for Parallel Magnetic Resonance Imaging (Ph.D. Thesis). Julius-Maximilians-University of Würzburg; 2006.

205. Bilgic B, Xie L, Dibb R, Langkammer C, Mutluay A, Ye H, Polimeni JR, Augustinack J, Liu C, Wald LL, Setsompop K. Rapid multi-orientation quantitative susceptibility mapping. NeuroImage. 2016; 125:1131–41. PMID: **26277773**. [PubMed: 26277773]

206. Renvall V, Witzel T, Wald LL, Polimeni JR. Fast variable inversion-recovery time EPI for anatomical reference and quantitative T1 mapping. Proc Intl Soc Mag Reson Med. 2014; 22:4282.

207. Beissner F, Polimeni JR, Bianciardi M, Renvall V, Eichner C, Napadow V, Wald LL. Imaging the human brainstem at 7 Tesla using multi-modal echo-planar imaging. Proc Intl Soc Mag Reson Med. 2014; 22:1413.

208. Olafsson V, Kundu P, Wong CW, Guo J, Lu K, Ghobrial E, Bandettini PA, Wong E, Liu T. Improved detection of BOLD-like Independent Components with Multi-Echo Simultaneous Multi-Slice acquisitions and Multi-Echo ICA. Proc Intl Soc Mag Reson Med. 2014; 22:4139.

209. Xu, J., Auerbach, E., Moeller, S., Martino, F. De, Yacoub, E., Ugurbil, K. Interleaved-TE fMRI acquisitions with highly accelerated Multiband EPI. 18th Annual Meeting of the Organization for Human Brain Mapping; 2012. p. 632

210. Dougherty, R., Mezer, A., Zhu, K., Kerr, A., Middione, M. Fast quantitative T1 mapping with Simultaneous Multi-Slice EPI. Annual Meeting of the Organization for Human Brain Mapping; 2014. p. 2002

211. Grinstead JW, Wang D, Bhat H, Deshpande V, Cauley SF, Setsompop K, Benner T, Anderson VC, Rooney WD. Slice-accelerated Inversion Recovery T1 mapping. Proc Intl Soc Mag Reson Med. 2014; 22:3215.

212. Ma D, Gulani V, Seiberlich N, Liu K, Sunshine JL, Duerk JL, Griswold MA. Magnetic resonance fingerprinting. Nature. 2013; 495(7440):187–92. PMID: **23486058**. [PubMed: 23486058]

213. Cloos MA, Wiggins CJ, Wiggins GC, Sodickson D. Plug and Play Parallel Transmission at 7 and 9.4 Tesla based on Principles from MR Fingerprinting. Proc Intl Soc Mag Reson Med. 2014; 144(2003):542.

214. Wong E. Optimized phase schedules for minimizing peak RF power in simultaneous multi-slice RF excitation pulses. Proc Intl Soc Mag Reson Med. 2012; 20:2209.

215. Auerbach EJ, Xu J, Yacoub E, Moeller S, Uğurbil K. Multiband accelerated spin-echo echo planar imaging with reduced peak RF power using time-shifted RF pulses. Magnetic Resonance in Medicine. 2013; 69(5):1261–7. PMID: **23468087**. [PubMed: 23468087]

216. Hennig J. Chemical shift imaging with phase-encoding RF pulses. Magnetic Resonance in Medicine. 1992; 25(2):289–298. PMID: **1614312**. [PubMed: 1614312]

217. Yao, C., Shen, L., Wu, J., Kritzer, M. Parallel Multi-slice Imaging with Limited Peak RF Power. Proceedings of the 12th Annual Meeting of SMRM; 1993. p. 427

218. Goelman G. Two methods for peak RF power minimization of multiple inversion-band pulses. Magnetic Resonance in Medicine. 1997; 37(5):658–665. PMID: **9126939**. [PubMed: 9126939]

219. Feinberg DA, Jakab PD. Tissue perfusion in humans studied by fourier velocity distribution, line scan, and echo-planar imaging. Magnetic Resonance in Medicine. 1990; 16(2):280–293. PMID: **2266847**. [PubMed: 2266847]

220. Reese TG, Heid O, Weisskoff RM, Wedeen VJ. Reduction of eddy-current-induced distortion in diffusion MRI using a twice-refocused spin echo. Magnetic Resonance in Medicine. 2003; 49(1): 177–82. PMID: **12509835**. [PubMed: 12509835]

221. Stejskal EO, Tanner JE. Spin diffusion measurements: spin echoes in the presence of a time-dependant field gradient. Journal of Chemical Physics. 1965; 42(1):288–292.

222. Zhu K, Kerr AB, Pauly JM. Nonlinear-Phase Multiband 90°–180° RF Pair With Reduced Peak Power. Proc Intl Soc Mag Reson Med. 2014; 22:1440.

223. Sharma A, Lustig M, Grissom WA. Root-flipped multiband refocusing pulses. Magnetic Resonance in Medicine. 2016; 75(1):227–237. PMID: **25704154**. [PubMed: 25704154]

224. Conolly SM, Nishimura DG, Macovski A, Glover GH. Variable-rate selective excitation. Journal of Magnetic Resonance. 1988; 78(3):440–458.

225. Eichner C, Wald LL, Setsompop K. A low power radiofrequency pulse for simultaneous multislice excitation and refocusing. Magnetic Resonance in Medicine. 2014; 72:949–58. PMID: **25103999**. [PubMed: 25103999]

226. Sharma A, Holdsworth SJ, O'Halloran R, Aboussouan E, Van AT, Maclaren J, Aksoy M, Stenger AV, Bammer R, Grissom WA. kT-PINS RF pulses for low-power field inhomogeneity-compensated multislice excitation. Proc Intl Soc Mag Reson Med. 2013; 21:44.

227. Cloos MA, Boulant N, Luong M, Ferrand G, Giacomini E, Le Bihan D, Amadon A. kT-points: short three-dimensional tailored RF pulses for flip-angle homogenization over an extended volume. Magnetic Resonance in Medicine. 2012; 67(1):72–80. PMID: **21590724**. [PubMed: 21590724]

228. Zhu Y. Parallel excitation with an array of transmit coils. Magnetic Resonance in Medicine. 2004; 51(4):775–84. PMID: **15065251**. [PubMed: 15065251]

229. Grissom WA, Yip C, Zhang Z, Stenger VA, Fessler JA, Noll DC. Spatial domain method for the design of RF pulses in multicoil parallel excitation. Magnetic Resonance in Medicine. 2006; 56(3):620–9. PMID: **16894579**. [PubMed: 16894579]

230. Katscher U, Börnert P, Leussler C, van den Brink JS. Transmit SENSE. Magnetic Resonance in Medicine. 2003; 49(1):144–50. PMID: **12509830**. [PubMed: 12509830]

231. Wu X, Schmitter S, Auerbach EJ, Moeller S, Uğurbil K, Van de Moortele P-F. Simultaneous multislice multiband parallel radiofrequency excitation with independent slice-specific transmit B1 homogenization. Magnetic Resonance in Medicine. 2013; 638:630–638. PMID: **23801410**.

232. Poser BA, Anderson RJ, Guerin B, Setsompop K, Deng W, Mareyam A, Serano P, Wald LL, Stenger VA. Simultaneous Multislice Excitation by Parallel Transmission. Magnetic Resonance in Medicine. 2014; 71:1416–1427. [PubMed: 23716365]

233. Wu X, Tian J, Schmitter S, Vaughan JT, Uğurbil K, Van de Moortele P-F. Z-stacked RF array design enhances parallel transmit multiband RF performance in whole brain simultaneous multislice. Proc Intl Soc Mag Reson Med. 2014; 22:543.

234. spectral-spatial E, Stenger VA. Fast-kz three-dimensional tailored radiofrequency pulse for reduced B1 inhomogeneity. Magnetic Resonance in Medicine. 2006; 55(4):719–24. PMID: **16526012**. [PubMed: 16526012]

235. Setsompop K, Wald LL, Alagappan V, Gagoski B, Hebrank F, Fontius U, Schmitt F, Adalsteinsson E. Parallel RF transmission with eight channels at 3 Tesla. Magnetic Resonance in Medicine. 2006; 56(5):1163–71. PMID: **17036289**. [PubMed: 17036289]

236. Anderson RJ, Poser BA, Grissom WA, Stenger VA. A Simultaneous Multi-Slice Fast-kz RF Pulse for Reduced B1+ Inhomogeneity. Proc Intl Soc Mag Reson Med. 2013; 21:2396.

237. Sharma A, Holdsworth SJ, O'Halloran R, Aboussouan E, Van AT, Aksoy M, Maclaren J, Bammer R, Stenger VA, Grissom WA. Multiband spokes pulses and design algorithm for B1+ inhomogeneity-compensated multislice excitation at 7T. Proc Intl Soc Mag Reson Med. 2013; 21:369.

238. Wu X, Uğurbil K, Van de Moortele P-F. Peak RF power constrained pulse design for multi-band parallel excitation. Proc Intl Soc Mag Reson Med. 2013; 21:4253.

239. Sharma A, Bammer R, Stenger VA, Grissom WA. Low peak power multiband spokes pulses for B1 (+) inhomogeneity-compensated simultaneous multislice excitation in high field MRI. Magnetic Resonance in Medicine. 2015; 74(3):747–55. PMID: **25203620**. [PubMed: 25203620]

240. Guérin B, Setsompop K, Ye H, Poser BA, Stenger AV, Wald LL. Design of parallel transmission pulses for simultaneous multislice with explicit control for peak power and local specific absorption rate. Magnetic Resonance in Medicine. 2015; 73(5):1946–53. PMID: **24938991**. [PubMed: 24938991]

241. Setsompop K, Wald LL, Alagappan V, Gagoski BA, Adalsteinsson E. Magnitude least squares optimization for parallel radio frequency excitation design demonstrated at 7 Tesla with eight channels. Magnetic Resonance in Medicine. 2008; 59(4):908–15. PMID: **18383281**. [PubMed: 18383281]

242. Yip C-Y, Yoon D, Olafsson V, Lee S, Grissom WA, Fessler JA, Noll DC. Spectral-spatial pulse design for through-plane phase precompensatory slice selection in T2*-weighted functional MRI. Magnetic Resonance in Medicine. 2009; 61(5):1137–47. PMID: **19267346**. [PubMed: 19267346]

243. Anderson RJ, Poser BA, Stenger VA. Simultaneous multislice spectral-spatial excitations for reduced signal loss susceptibility artifact in BOLD functional MRI. Magnetic Resonance in Medicine. 2014; 72(5):1342–52. PMID: **24338863**. [PubMed: 24338863]

244. Sharma A, Donahue MJ, Stenger VA, Grissom WA. SALSAS: Spectral spatial excitation combined with z-shimming to mitigate through-plane signal loss in single-slice and multiband gradient echo imaging. Proc Intl Soc Mag Reson Med. 2014; 22:1479.

245. Wu X, Vu AT, Schmitter S, Auerbach EJ, Moeller S, Lenglet C, Yacoub E, Van de Moortele P-F. Whole brain single shot diffusion weighted EPI at 7 Tesla using parallel transmit multislice multiband RF pulses. Proc Intl Soc Mag Reson Med. 2014; 22:311.

246. Schmitter S, Wu X, Moeller S, Wang D, Greiser A, Auerbach EJ, Delabarre L, Van de Moortele P-F. Multi-Band-Multi-Spoke pTX RF Pulse Design in the Heart at 7 Tesla: towards Faster, Uniform Contrast Cardiac CINE Imaging. Proc Intl Soc Mag Reson Med. 2014; 22:646.

247. Stockmann JP, Witzel T, Keil B, Mareyam A, Polimeni JR, LaPierre C, Wald LL. A 32ch combined RF-shim brain array for efficient B0 shimming and RF reception at 3T. Proc Intl Soc Mag Reson Med. 2014; 22:400.

248. Truong T-K, Darnell D, Song AW. Integrated RF/shim coil array for parallel reception and localized B0 shimming in the human brain. NeuroImage. 2014; 103:235–40. PMID: **25270602**. [PubMed: 25270602]

249. Juchem C, Nixon TW, McIntyre S, Boer VO, Rothman DL, de Graaf RA. Dynamic multi-coil shimming of the human brain at 7 T. Journal of Magnetic Resonance. 2011; 212(2):280–8. PMID: **21824794**. [PubMed: 21824794]

250. De Zanche N, Barmet C, Nordmeyer-Massner JA, Pruessmann KP. NMR probes for measuring magnetic fields and field dynamics in MR systems. Magnetic Resonance in Medicine. 2008; 60(1):176–86. PMID: **18581363**. [PubMed: 18581363]

251. Duerst Y, Wilm BJ, Dietrich BE, Vannesjo SJ, Barmet C, Schmid T, Brunner DO, Pruessmann KP. Real-time feedback for spatiotemporal field stabilization in MR systems. Magnetic Resonance in Medicine. 2015; 73(2):884–93. PMID: **24634192**. [PubMed: 24634192]

252. Kasper L, Bollmann S, Vannesjo SJ, Gross S, Haeberlin M, Dietrich BE, Pruessmann KP. Monitoring, analysis, and correction of magnetic field fluctuations in echo planar imaging time series. Magnetic Resonance in Medicine. 2015; 74(2):396–409. PMID: **25123595**. [PubMed: 25123595]

253. Poser BA, Ivanov D, Kemper VG, Kannengiesser SA, Uludag K, Barth M. CAIPIRINHA-accelerated 3D EPI for high temporal and / or spatial resolution EPI acquisitions. Proc Euro Soc Magn Reson Med B (Toulouse, France). 2013:226.

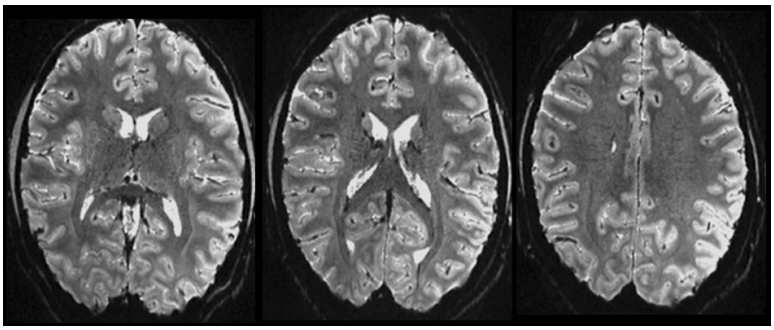

Fig. 1.

Example 0.75 mm isotropic single-shot BOLD-weighted gradient-echo EPI acquired at 7T, using *R*=3 acceleration, GRAPPA reconstruction, a 32-channel receive coil array, and a head gradient coil. (The mean of five time points is shown.) The acceleration reduces the effective echo spacing enough that only minor geometric distortions are present.

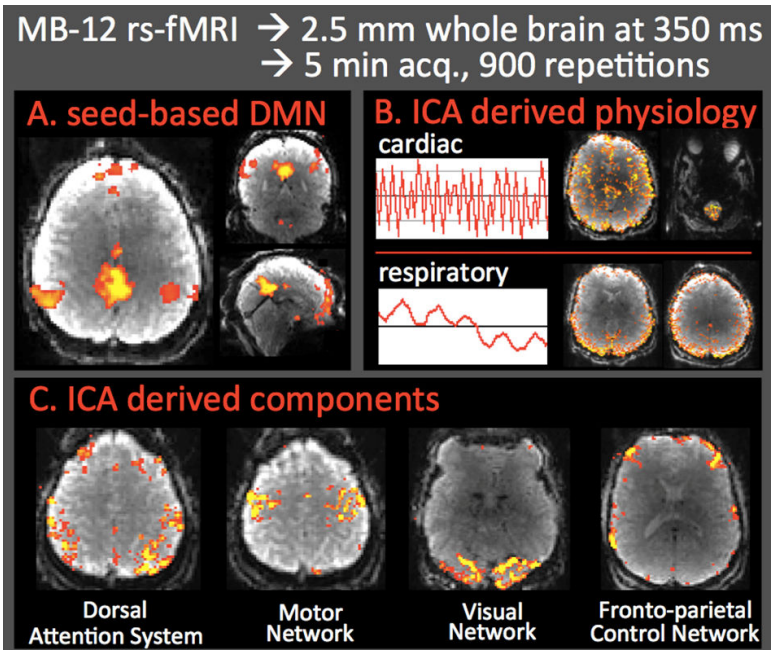

Fig. 2.

MB-12 resting-state fMRI using a 64-channel coil on the 3T "Connectom" system. (A) The DMN from standard seed-based analysis with 4 mm FWHM smoothing, lowpass filtered at 0.08 Hz. (B, C) ICA on same data. (B) Time courses of cardiac and respiratory components and corresponding ICs. The cardiac component is seen within the spinal cord and throughout the brain likely within large vessels and CSF regions. (C) Major global networks from ICA with 2 mm FWHM smoothing. These components are well-confined to gray matter.

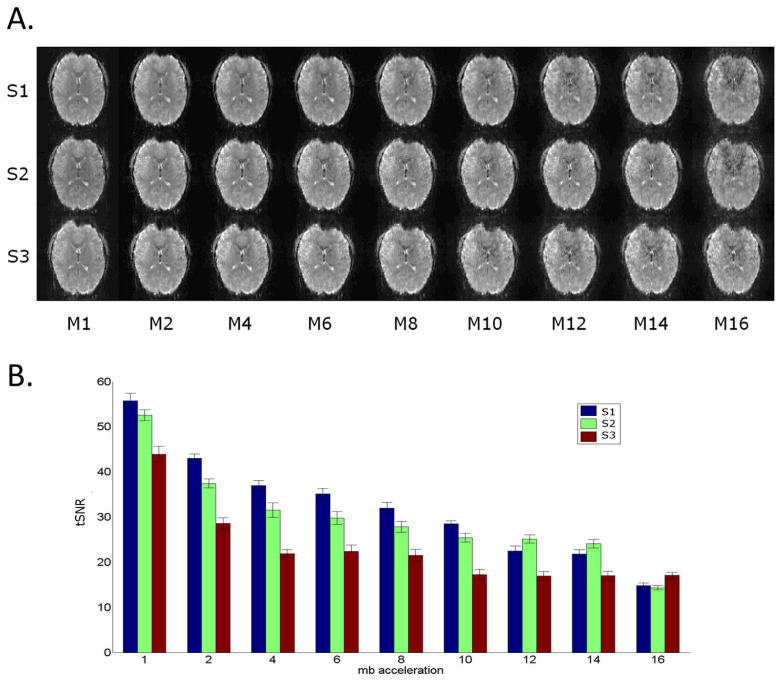

Fig. 3.

(A) Representative slices from one subject with multiplexed-EPI using different *S* and *M* (SIR and MB) factors at constant TR = 500 ms. From top to bottom: *S* factors are 1, 2 and 3. From left to right: *M* factors are 1, 2, 4, 6, 8, 10, 12, 14 and 16. (B) tSNR comparisons of constant TR acquisitions averaged across seven subjects. (Reproduced from Ref. [57].)

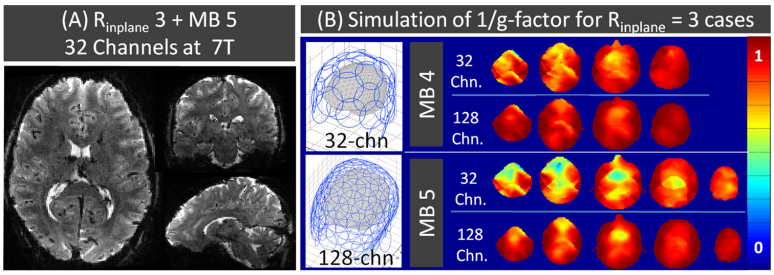

Fig. 4.

(A) 15. (MB-5, R=3) accelerated 1.5 mm iso. SMS-EPI acquisition using a custom 32-channel coil array at 7T. (B) Simulation of 1/g-factor maps, comparing performance of 32-channel and 128-channel coil arrays at 7T, for MB-4 and MB-5 acquisitions, both with inplane acceleration of 3.

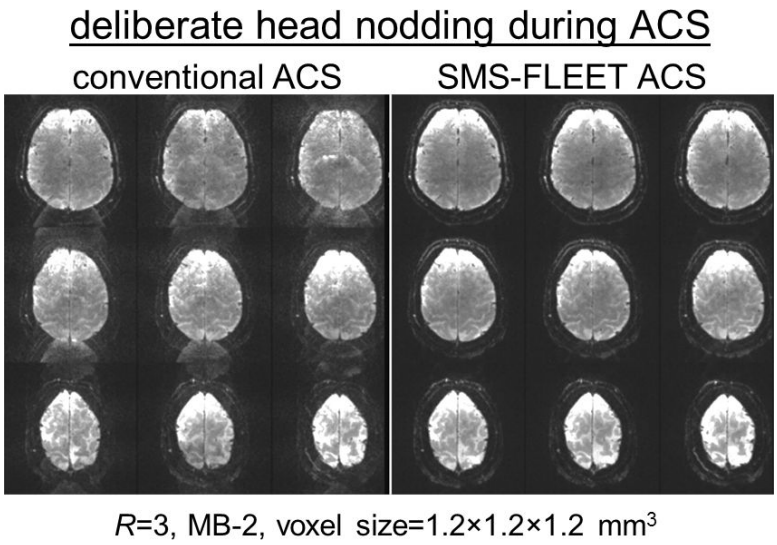

Fig. 5.

FLEET ACS reduces sensitivity of PI calibration to motion. SMS-EPI images (R=3, MB-2, voxel size=1.2×1.2×1.2 mm^3) reconstructed after subject was instructed to nod their head only during the ACS acquisition. The images reconstructed using conventional multi-shot EPI ACS data exhibit strong aliasing artifacts as well as cross-slice contamination. (Reproduced from Ref. [78].)

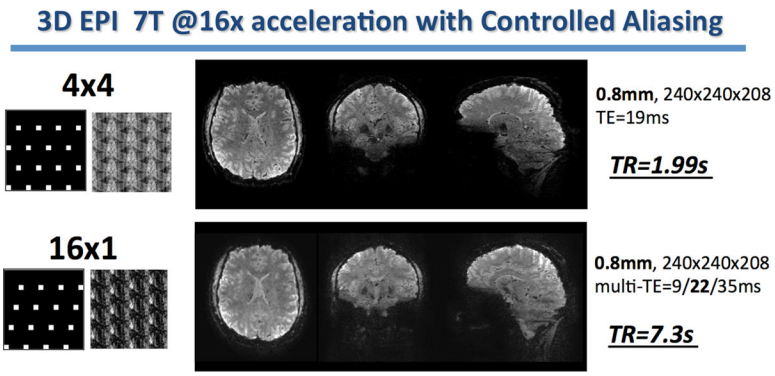

Fig. 6.

3D-EPI at 7T at 16× acceleration using 2D-CAIPI. Two different acceleration strategies are shown for $R_y \times R_z$ = 4×4 (top row) and 16×1 (bottom row). In each row, k-space under-sampling and the spatial aliasing patterns are shown on the left, along with the resulting un-aliased imaging volume and imaging parameters on the right. With 4×4 acceleration, 0.8 mm isotropic data can be acquired in only 1.99 s with low levels of geometric distortion. In the 16×1 acceleration case, imaging speed is traded off for echo spacing to provide very low distortion and a short echo-train length of 12 ms, which enabled a multi-echo acquisition with 3 echoes. (Reproduced from Ref. [253].)

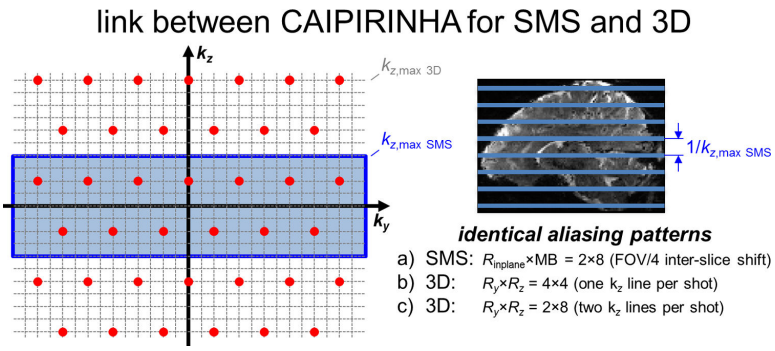

Fig. 7.

The link between CAIPIRINHA sampling for SMS and 3D acquisitions for a particular 16× undersampling pattern. In SMS-EPI, blipped-CAIPI sampling can be used to acquire data in the blue highlighted region to achieve an acquisition with acceleration R_{inplane}×MB = 2×8 with an inter-slice image shift of FOV/4 (corresponding to FOV/2 in the reduced inplane FOV). For 3D-EPI, the full 3D k-space must be acquired using multiple EPI shots. For this, multiple acceleration options are possible, depending on the number of k_z lines that are to be acquired per EPI readout, e.g. R_y×R_z = 4×4 with one k_z line per EPI, or R_y×R_z = 2×8 with two k_z lines per EPI to reduce the number of EPI shots needed by 2×. The first example will result in a 50% reduction in B_0 inhomogeneity related image distortion when compared to the SMS-EPI acquisition, while in the later will have identical image distortion. Note that in all cases, the final full k-space sampling pattern is the same, leading to identical aliasing pattern as in the blipped-CAIPI case with images from eight slices equally spread along the partition encoding direction, aliasing onto one another with inplane aliasing factor of 2 and FOV/4 inter-slice shift.

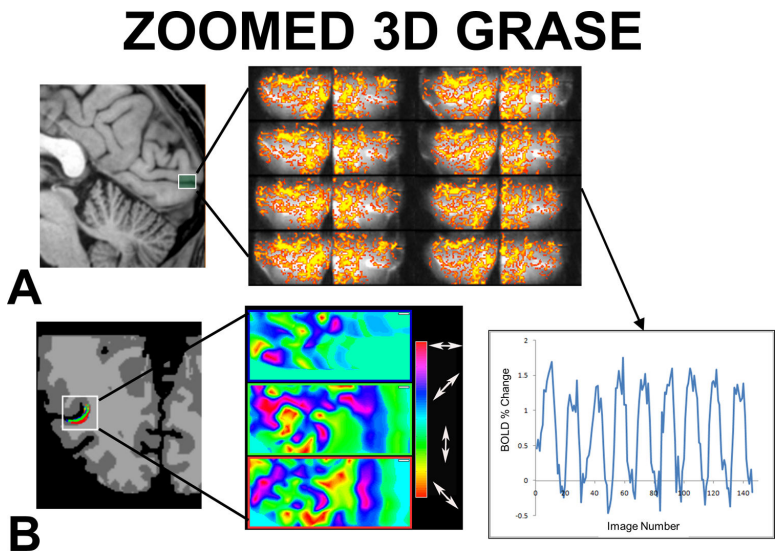

Fig. 8.

(A) Zoomed inner-volume single-shot 3D-GRASE images acquired at 0.7 mm isotropic resolution in the primary visual cortex at the calcarine fissure (box) during visual stimulation with a flickering checkerboard, with the corresponding time course (in units of percent signal change) shown on right. (B) Columnar architecture in visual cortical area MT revealed with 3D-GRASE. The preferred axis-of-motion orientation of voxels at three different cortical depths in the Superior Temporal Sulcus (STS) (left) was measured with zoomed 3D-GRASE. The color maps indicate preferred orientation across three cortical depths. (Reproduced from Ref. [112].)

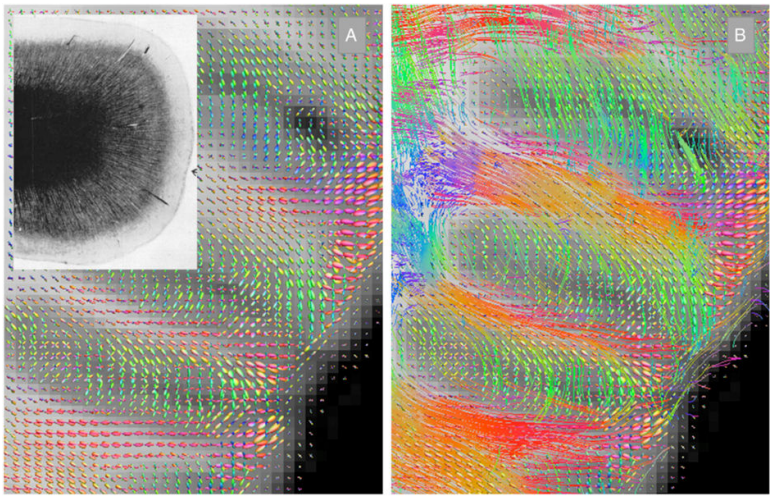

Fig. 9.

Fiber orientation density plots (A) and streamline tracking (B) of sub-millimeter isotropic resolution (800 μm) Diffusion MRI data in horizontal slice through parietal lobe, showing white matter fiber tracts entering the cortex. See inset for myeloarchitecture of a gyrus for qualitative comparison. Diffusion MRI data were acquired using ZOOPPA, where 3/4 brain acquisition at 800 μm would take approximately 65 min. (Reproduced from Ref. [141].)

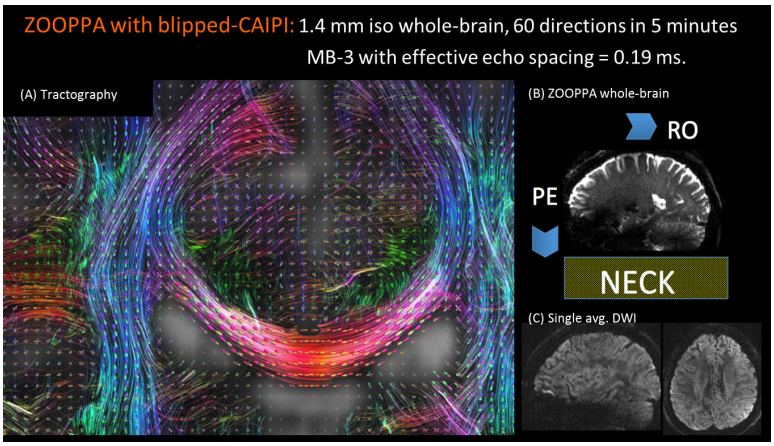

Fig. 10.

Combination of ZOOPPA and blipped-CAIPI SMS-EPI enables low-distortion, high-resolution, whole-brain diffusion imaging to be acquire rapidly. (A) Tractography result from 1.4 mm isotropic data acquired in 5 min using MB-3, (B) ZOOPPA with OVS applied to the neck to enable whole-brain acquisition with low distortion at effective echo-spacing of 0.19 (R_{GRAPPA}=2, R_{ZOOM}=1.8, thus R_{total}=3.6). (C) Single-average diffusion imaging data.

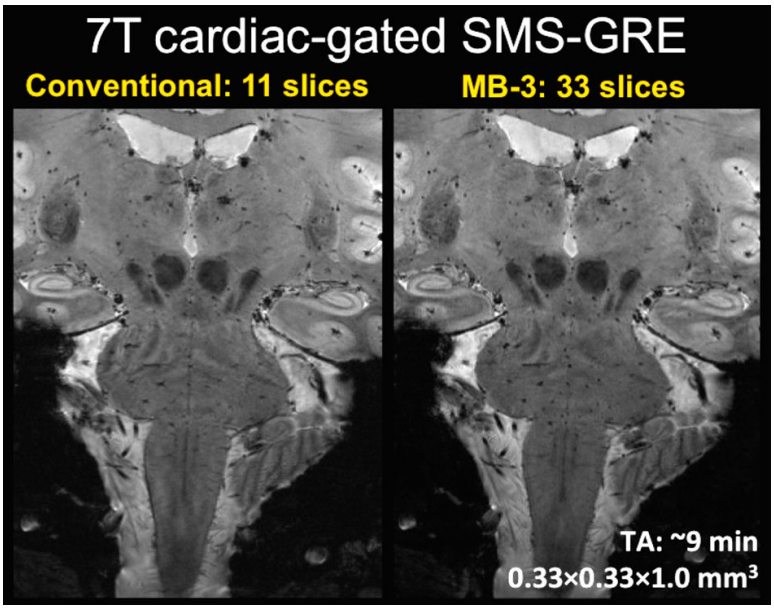

Fig. 11.

High-resolution brainstem and basal ganglia T_2*-weighted imaging at 7T using SMS-GRE with cardiac gating and phase stabilization (TE=21 ms, TR=900 ms, nominal TR (cardiac window) = 457 ms, 576×576 matrix, voxel size=0.33×0.33×1.0 mm^3, BW=30 Hz/pixel). Similar high-quality depiction of the anatomical structures can be seen in the conventional slice-interleaved acquisition and in the MB-3 acquisition (using an FOV/2 CAIPI shift and slice-GRAPPA reconstruction).

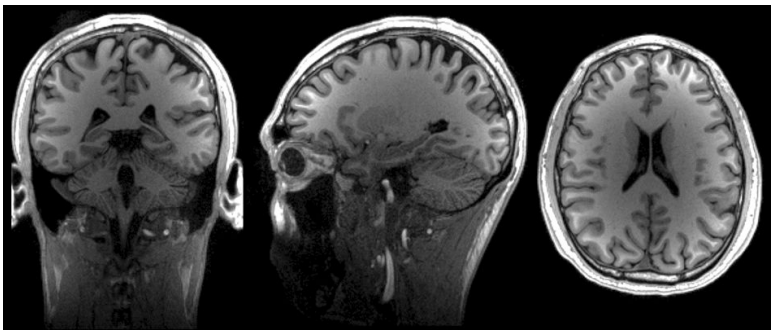

Fig. 12.

Example 1 mm isotropic CAIPI-MEMPRAGE (4 echoes, R_{pe}=3, R_{par}=2, CAIPI shift=1) acquired at 3T with a 32-channel head coil array and online image reconstruction (without intensity normalization). The conventional outer-loop acceleration provided a short scan time of 3:52 min, while the 2-fold inner-loop acceleration reduced the effective echo-spacing from 9.4 ms to 4.7 ms. Separate FLASH-based reference lines were used to increase time efficiency.

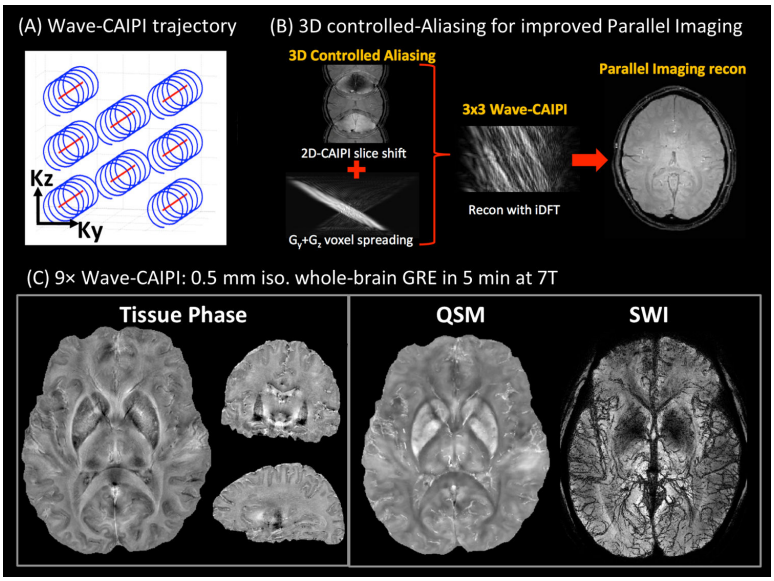

Fig. 13.

Wave-CAIPI applied to high-resolution QSM. (A) Undersampled k-space trajectory used in 9× accelerated wave-CAIPI acquisition. (B, *left*) 3D controlled aliasing from Wave-CAIPI with inter-slice shift from 2D-CAIPI and voxel spreading from G_y and G_z sinusoidal gradients. (B, *center*) 9× accelerated Wave-CAIPI with direct inverse Fourier transform (iDFT) reconstruction demonstrating complex aliasing pattern. (B, *right*) High-quality reconstruction achieved by incorporating a point spread function model into SENSE-based PI reconstruction. (C) Tissue phase, QSM, and SWI results from 9× accelerated 0.5 mm isotropic acquisition at 7T.

Table 1

High-level summary of the major trends/directions of sequence development at ultra-high field, and the key benefits from these new acquisition technologies.

Sequence development directions
i) Transition from 2D to SMS and 3D imaging
- Improved SNR through volumetric noise averaging
- Parallel imaging in multiple spatial dimensions
- *Improved parallel imaging with better control of aliasing*
Methods:
→ CAIPI, 2D-CAIPI, BPE/Zig-Zag, Wave-CAIPI
ii) Rapid encoding for artifact reduction in EPI, spiral, 3D-EPI
- Reduced distortion, reduced image blurring, shorter TE
Methods:
→ Zoomed/Reduced FOV: IVI, OVS, multidimensional RF
→ Multi-shot/Segmented: RS-EPI, Multishot-EPI, 3D-EPI, GRASE, 3D-GRASE
→ Parallel Imaging inplane acceleration
Benefits from these developments
- Increased spatial resolution with reductions in blurring, distortion, and motion
- Improved spatial-temporal resolution trade-off
- Increased brain coverage
- Improved encoding-intensive multi-contrast/quantitative imaging: MultiEcho-EPI, MultiInv-ASL, MultiOrientation-QSM, T_1-EPI, MEMPxRAGE